

Multi-Objective Optimization of Stress Concentration Factors for Fatigue Design of Internal Ring-Reinforced KT-Joints Undergoing Brace Axial Compression

Adnan Rasul ^{1*}, Saravanan Karuppanan ¹, Veeradasan Perumal ¹,
Mark Ovinis ², Mohsin Iqbal ¹

¹ Department of Mechanical Engineering, Universiti Teknologi PETRONAS, Seri Iskandar 32610, Malaysia.

² School of Engineering and the Built Environment, Birmingham City University, Birmingham, United Kingdom.

Received 20 February 2024; Revised 20 May 2024; Accepted 25 May 2024; Published 01 June 2024

Abstract

Stress concentration factors are important to determine fatigue life based on the S-N curve methodology, where the lower the stress concentration factor, the higher the fatigue life. In this work, we developed internal ring-reinforced KT-joints, one of the most commonly used joints in the offshore industry, for the most practical ranges with the least stress concentration factors, followed by the formulation of a novel set of parametric equations for determining the stress concentration factors of internal ring-reinforced KT-joints. Using numerical investigation based on a finite element model and a response surface approach with 8 parameters (λ , δ , ψ , ζ , θ , τ , γ , and β) as input and eleven outputs (SCF 0° to SCF 90° and peak SCF), the stress at ten locations around the brace was evaluated, since efficient response surface methodology has been proven to give comprehensive and accurate predictions. The KT-joint with the following parameters: $\lambda=0.951515$, $\delta=0.2$, $\psi=0.8$, $\zeta=0.31$, $\theta=45.15^\circ$, $\tau=0.60$, $\gamma=16.25$, and $\beta=0.40$ had the least stress concentration factor. The KT-joint with the optimized parameters was validated through finite element analysis. The resulting percentage difference was less than 6%, indicating the applicability of the response surface methodology with high accuracy.

Keywords: KT-joint; Response Surface Methodology; Stress Concentration Factor; Ring-Stiffeners; Fatigue; Multi-Objective Optimization; Finite Element Analysis.

1. Introduction

Jacket type offshore platforms are created from circular hollow sections (CHS) tubular segments via welding the branching component (brace) to the main structure (chord), creating tubular joints. The KT-joint is among the most commonly employed tubular joints. It has a complex shape, as shown in Figure 1-a. Three circular braces are welded to the main chord in the KT joint. The central brace is 90° to the chord, while the outer inclined braces are at an angle θ to the main chord.

Alternatives such as internal rings are considered if the joint's capacity is insufficient during the development phase. The rings are joined by welding within the chord, which substantially improves load-bearing ability, reduces stress concentration factors, increases fatigue life, and prevents wave forces and corrosive attacks [1]. These are called internal ring-reinforced joints, or stiffeners, as shown in Figure 1-b.

* Corresponding author: adnan_22006634@utp.edu.my

<http://dx.doi.org/10.28991/CEJ-2024-010-06-03>



© 2024 by the authors. Licensee C.E.J, Tehran, Iran. This article is an open access article distributed under the terms and conditions of the Creative Commons Attribution (CC-BY) license (<http://creativecommons.org/licenses/by/4.0/>).

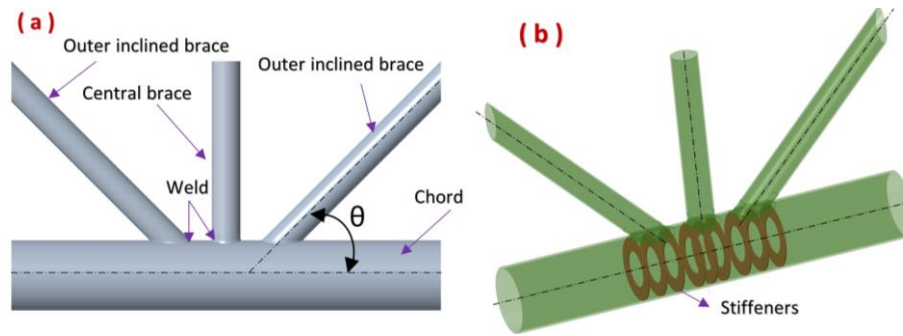


Figure 1. a) A typical Tubular KT joint, b) internally ring stiffened KT-joint

Three methods are frequently employed in the analysis of fatigue in tubular joints. These are the experimental approach, the fracture mechanics (FM)-based approach, and the S–N curve-based approach. The experimental approach involves physical experiments to quantitatively assess the fatigue characteristics exhibited by tubular joints when subjected to cyclic loads. The fracture mechanics approach considers crack propagation and is mostly employed for pre-existing structures with a fracture within an existing joint.

In the S–N curves-based approach, the number of cycles to failure (N) is based on the hotspot stress (HSS). The S–N curve is a widely employed technique for assessing the fatigue life of tubular joints [2]. Engineers estimate the fatigue life of tubular joints based on the HSS and S–N curves [3]. The HSS is the site at which a crack caused by fatigue is most likely to initiate [4].

The SCF, the ratio of hotspot stress to nominal stress, is used to assess the extent of stress concentration. It is dependent upon various factors, including joint geometry, loading conditions, weld size and type, and proximity to the weld. In the last five decades, extensive research has been dedicated to the establishment of precise parametric equations for stress concentration factors (SCFs), as they serve as a fundamental component in the computation of fatigue life [5–7]. These equations provide SCF under various loading circumstances, often through experimental research and comprehensive finite element analysis (FEA).

Structural failure can happen when a given structure becomes incapable of withstanding the applied stresses or forces. Offshore structures are subjected to a variety of complex environmental loads, such as earthquakes, ice and mud, ice and waves, buoyancy, and storms [8]. With at least 2,000 ring-stiffened joints only in the North Sea, there is a strong requirement for strength and SCF calculation guidance [9].

Several scholars [5–7] have utilized findings from experimental studies and finite element analysis (FEA) to develop their formulations. The literature has focused on the stress concentration factors of KT-joints with less emphasis on fatigue life enhancement, especially the optimization of stress concentration factors of tubular joints.

1.1. Reduction of Stress Concentration Factors with Internal Rings

Recent publications have shown that internal rings can reduce stress concentration factors. According to Ahmadi et al. [10], internal ring-stiffeners (IRS) may cause the peak SCF to be located around the weld toe, depending on the geometrical factors. Additionally, the SCF distributions in the stiffened and unstiffened joints may have very distinct forms. SCFs in an unstiffened KT joint are often greater than SCFs in a similar IRS joint at the same places.

By comparing the SCFs of unstiffened tubular joints with stiffened tubular KK-joints, Pan et al. [11] concluded that the maximum SCF reductions at saddle point, crown point, and peak point are 82%, 53%, and 63%, respectively. According to Ahmadi et al. [1], increasing stiffener width decreases the SCF at both saddle and crown positions in internally stiffened TT joints. By analyzing internal ring-reinforced tubular T-joints, Krishna & Nallayarasu [12] concluded that the reduction in SCF of saddle and crown position was 75% and 20%, respectively. The spacing ratio and location of rings have a more significant influence on the SCFs.

Recent studies, including work by Ahmadi et al. [1] and Pan et al. [11], demonstrate that internal rings, especially in tubular joints, effectively reduce stress concentration factors (SCFs). The research indicates that factors such as geometrical considerations and stiffener width, spacing ratio, and location of rings play a crucial role in SCF distribution. Findings suggest significant SCF reductions, with Pan et al. [11] reporting up to 82% reduction at specific points in internally stiffened KK-joints.

2. Literature Review

The KT-joint is frequently employed and has been extensively researched. This section contains the latest research studies on the KT joint and internally ring-reinforced KT-joint. Kaung et al. [13] provided parametric equations for

determining the stress concentration factors for Y, T, KT, and K-joints based on a finite element program. The Kuang equations were developed by statistical analysis of data acquired during the study of FE joints. The exact location of the hot-spot stress around the weld is unknown; instead, it is classified as chord-side or brace-side. The equations do not account for the effect of chord length on the saddle due to restrictions at the chord's ends. Therefore, it is likely that the SCFs for chord lengths with greater chord lengths (α) are underestimated as a result of Kuang's predominantly shorter chord length joints [14].

The UK Health and Safety Executive commissioned a study [15] to create a databank of in-service ring-stiffened joints and, using the in-service data, to uncover the uncertainties related to the design (strength and fatigue both) of such joints. The research has brought attention to the insufficiency of the elastic closed-ring analysis technique, which is frequently employed by consulting engineers and operators to determine the capacity of ring-stiffened joints [9]. Ahmadi et al. [10] conducted the experimental and numerical investigation of geometric SCFs in offshore structures' internal ring-stiffened tubular KT joints to develop a novel set of SCF parametric equations for the fatigue design of internal ring-reinforced KT joints based on the parameter depth of internal rings and joint geometry. The effects of the spacing ratio and thickness of the rings were not investigated. The spacing ratio and thickness of rings have a significant effect on reducing the SCF [16]. Azari Dodaran et al. [17] investigated the effect of geometry on the static strength of axially loaded tubular KT joints at high temperatures and suggested parametric equations. For evaluating the SCFs of unstiffened KT-joints, parametric equations were proposed by Lotfollahi-Yaghin et al. [18]. They concluded that the geometrical parameter values affect the distribution of SCFs surrounding the weld toe and the hot spot stress (HSS) position. As a result, the HSS might not always be found in the saddle or crown area.

Hamid Ahmadi et al. [4, 10, 19–24] developed SCF parametric equations, performed significant work on the internal ring stiffened KT-joint, and concluded that internal ring stiffeners could considerably reduce SCF. They conducted a numerical analysis for the chord-side SCF [24] after conducting an experimental and numerical investigation for the geometric SCF of the central brace under axial load [10]. They study the probability distribution of SCFs under axial [20], IPB [21], and OPB [19] loadings. They further studied the outer brace SCF parametrically [4]. They also investigated SCF because of in-plane bending [23] and out-of-plane bending [22].

Sadat Hosseini et al. [25] used fiber-reinforced polymer (FRP) material to reinforce the KT joint. They employed three distinct FRPs and three different epoxies to perform parametric research on 1458 FE models subjected to three axial brace loading situations. According to Iqbal et al. [26], the FRP can significantly lower the stress intensity factor of semi-elliptical cracks in KT-joints. Aidibi et al. [27] performed a comparative study based on numerical investigations for the SCF of KT joints. After considering various loadings, they concluded that the SCFs derived through numerical studies are more conservative than those acquired through analytical research. They used MATLAB and Python scripting for the extraction of SCF and HSS. They performed nonlinear regression analysis and developed an equation for calculating SCF under bending stresses. Peak hotspot stress (HSS) and SCF subjected to combined axial, in-plane, and out-of-plane bending loads and their placement around the central brace were analytically studied by Iqbal et al. [6, 28]. They employed empirical models to calculate SCF around the central brace.

Despite extensive research on the internal ring re-enforced KT-joint for the determination of SCFs [4, 10, 22–24], the literature evaluation indicates a lack of research on three main factors. Firstly, the stress concentrations of internal rings stiffened KT-joints with two important parameters [16], i.e., the parameters related to spacing ratio and thickness of the rings, have not been investigated. Investigations of the effect of the parameters related to the spacing ratio and thickness of the rings are crucial, as they play an important role in the SCF values and shapes [16]. Secondly, no equations are available to determine the SCF of internal ring-reinforced joints, including these two parameters. Major offshore design codes like API-RP2A-WSD [29] and DNV-RP-C203 [30] do not include detailed quantitative recommendations for ring-stiffened joints. Thirdly, the literature lacks optimization of these SCFs, as minimizing these SCFs enhances the fatigue life of tubular joints [31]. Since efficient response surface methodology (RSM) has been proven to give comprehensive and accurate predictions [32], this research aims to fulfill these objectives using RSM. The effects of these parameters are studied, and a novel set of equations is proposed, which includes all the ring parameters. Finally, by validating the optimization output with FEA analysis results, we are able to achieve an internally reinforced KT-joint with the lowest Stress Concentration Factor (SCF) and excellent accuracy.

3. Research Methodology

The methodology involves the parametric modeling in CREO 5.0 software before finite element modeling in ANSYS workbench 2021, followed by analyzing the response surface design and optimization in Minitab software. The methodology flow chart is shown in Figure 2. Each step is explained in the following sections.

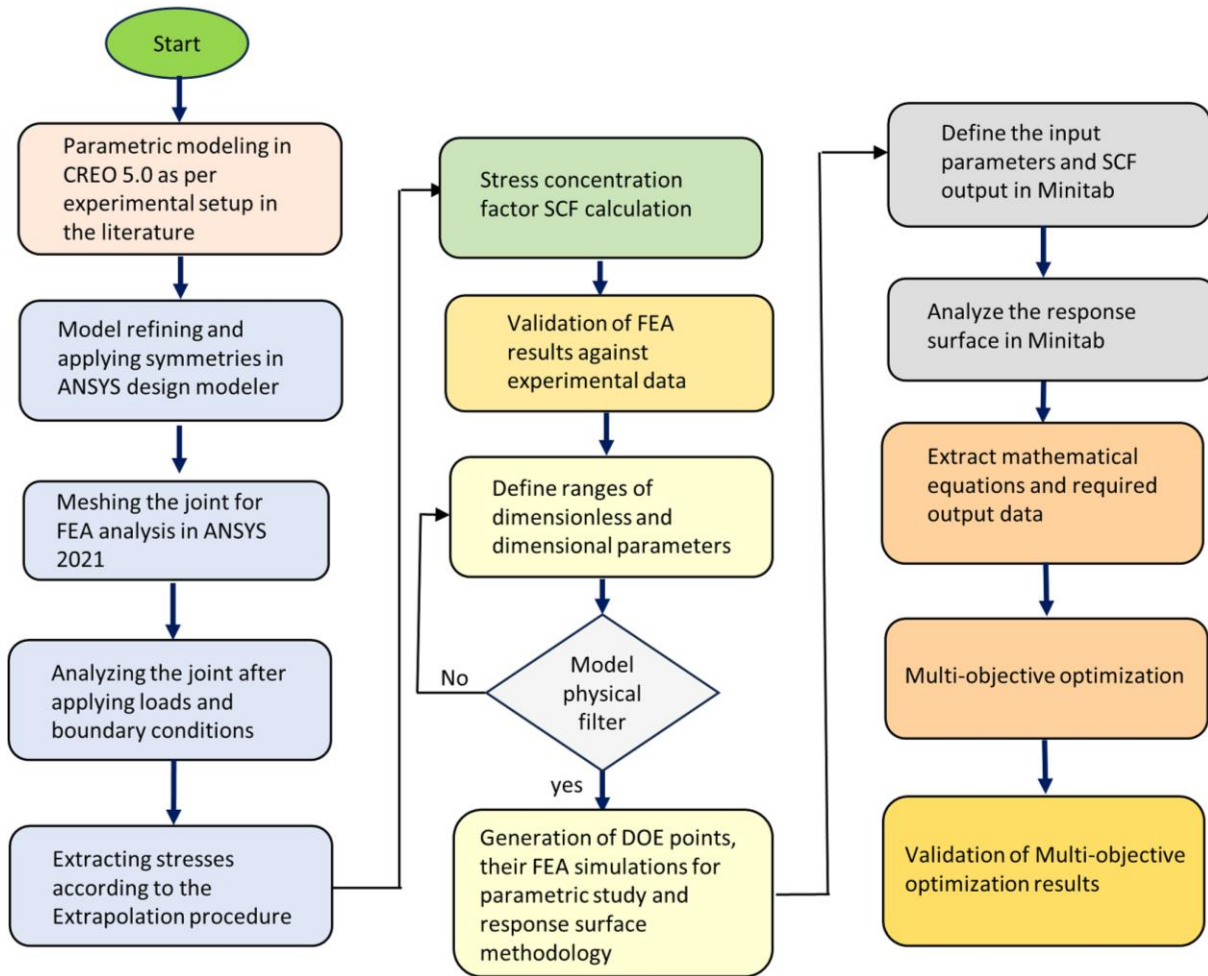


Figure 2. Methodology Flowchart

3.1. Finite Element Modeling

Based on the published experimental research by Ahmadi et al. [4, 10, 19-24], a KT joint was modeled in Creo 5.0. They used two identical KT joints, one with internal rings welded inside the chord and the other a KT joint with no stiffening. Three rings were used in the current investigation for each brace, as illustrated in Figure 3. Two were joined at crown positions, with the third at the saddle location. Parametric modeling was performed in CREO 5.0 software based on the dimensionless parameters in Equations 1 to 9 in Figure 3. The notations and definitions associated with particular terms are provided in the "Nomenclature" section.

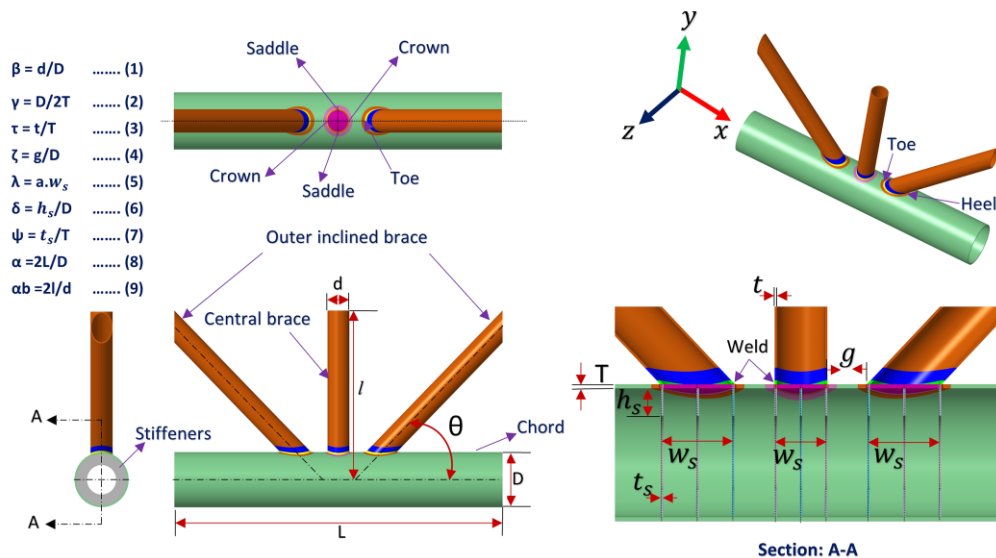


Figure 3. Parametric modeling in CREO 5.0

According to N'Diaye et al. [33], linear elastic static analysis is appropriate for calculating the SCFs in tubular joints. The material selected for the KT-joint and stiffeners is steel, which has a Young's modulus of 207 GPa and a Poisson's ratio of 0.3 [5, 25].

As shown in Figure 3, the parts were modeled in pieces and then assembled, which helped achieve sub-zone meshing, as explained in the next section. Due to the parametric modeling and efficient CREO 5.0 software, the model creation, update, and saving for the next iteration take about 30 seconds. The welding profile needs careful attention for an accurate measurement of SCF. The size around the brace and chord junction is based on the AWS D 1.1 specifications (2020), and the weld profile is modeled according to AWS D 1.1 [34], as explained by Lotfollahi et al. [18].

For FEA analysis, the model was imported into the ANSYS 2021 software. Only 1/4 of the complete KT-joint is required to be modeled due to the XY-plane and YZ-plane symmetries in the joint geometry and loading. Symmetries and model refinement were done in the ANSYS design modeler. The parts were modeled in pieces to achieve the best configuration for mesh generation. They were assembled in CREO 5.0 to achieve the best mesh for the KT-joint analysis, as shown in Figure 4.

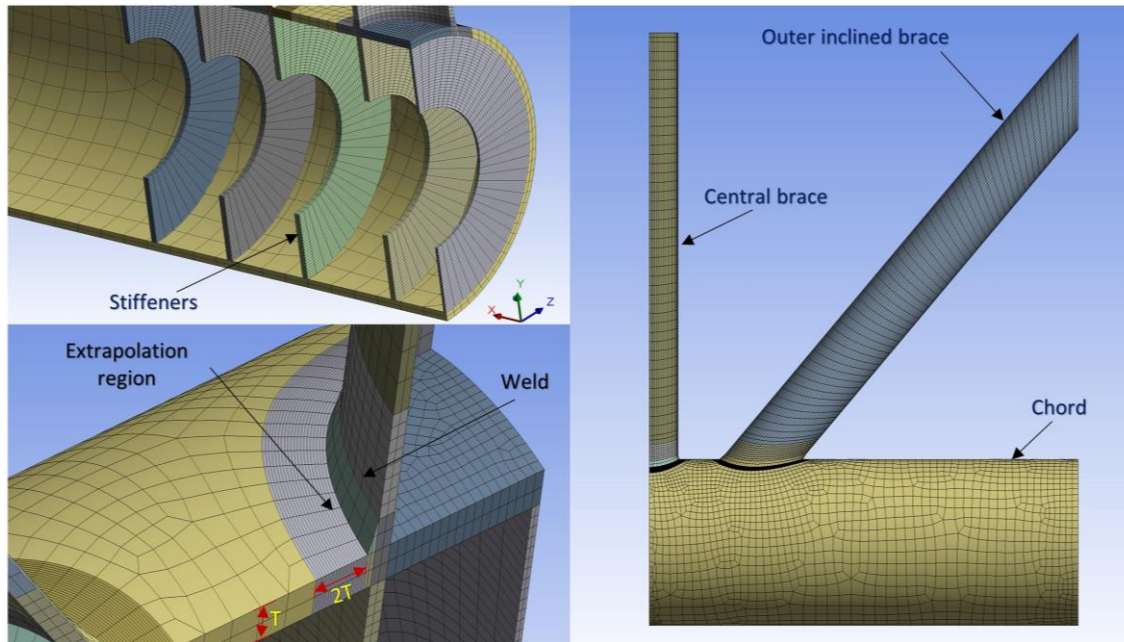


Figure 4. Mesh generated for FEA analysis of KT-joint in ANSYS 2021

A sensitivity assessment led to the finalization of a mesh of 12799 elements. For the mesh generation of the model, a sub-zone method was employed to achieve better results. The extrapolation region was meshed in such a way to obtain nodes at 10° around the brace. The chord braces and stiffeners were meshed separately, and ANSYS contacts were used for their connections.

A 500 kN-capacity actuator was used to apply a static load at the top of the central brace in the experiment [4, 10, 19–24]. The specimen's deformation should be kept linearly elastic by carefully selecting the load magnitudes [24]. Figure 5 illustrates the loads and boundary conditions implemented in the experimental investigation conducted by Ahmadi et al. [3]. Both ends of the chord and the outer inclined brace were fixed. A static force of 71.7 kN was exerted at the top of the central brace, as shown in Figure 5 [4, 10, 19–24].

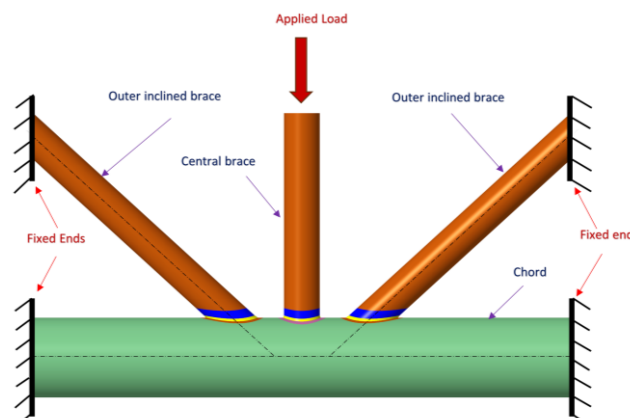


Figure 5. Applied loads and boundary conditions

3.2. Stresses and SCF Calculation

The stress concentration factors (SCFs) were calculated using the method established by the International Institute of Welding IIW-XVE [35]. The von Mises stresses were linearly extrapolated at two points at distances of 0.4T and 1.4T from the weld toe, where T represents the thickness of the chord. Von Mises stress was also used for SCF calculation in the work by [36–38]. Due to the complicated shape of the weld toe, the SCF zone was meshed separately, and the length of the SCF zone was selected as twice the thickness of the chord so that the node at 1.4T is not affected by mesh size of the chord outside extrapolation region and to get the nodes at a distance of 0.1T. For extrapolation points around the brace, the extrapolation region from 0° to 90° was divided into 18 equal portions to get the stresses at an angle of 10° from the crown position to the saddle position, as shown in Figure 6. After getting the von Mises stresses at the fourth and fourteenth elements, the hotspot stress at the weld toe was extrapolated accordingly. The SCF was then determined by dividing the hotspot stress by the nominal stress at the brace.

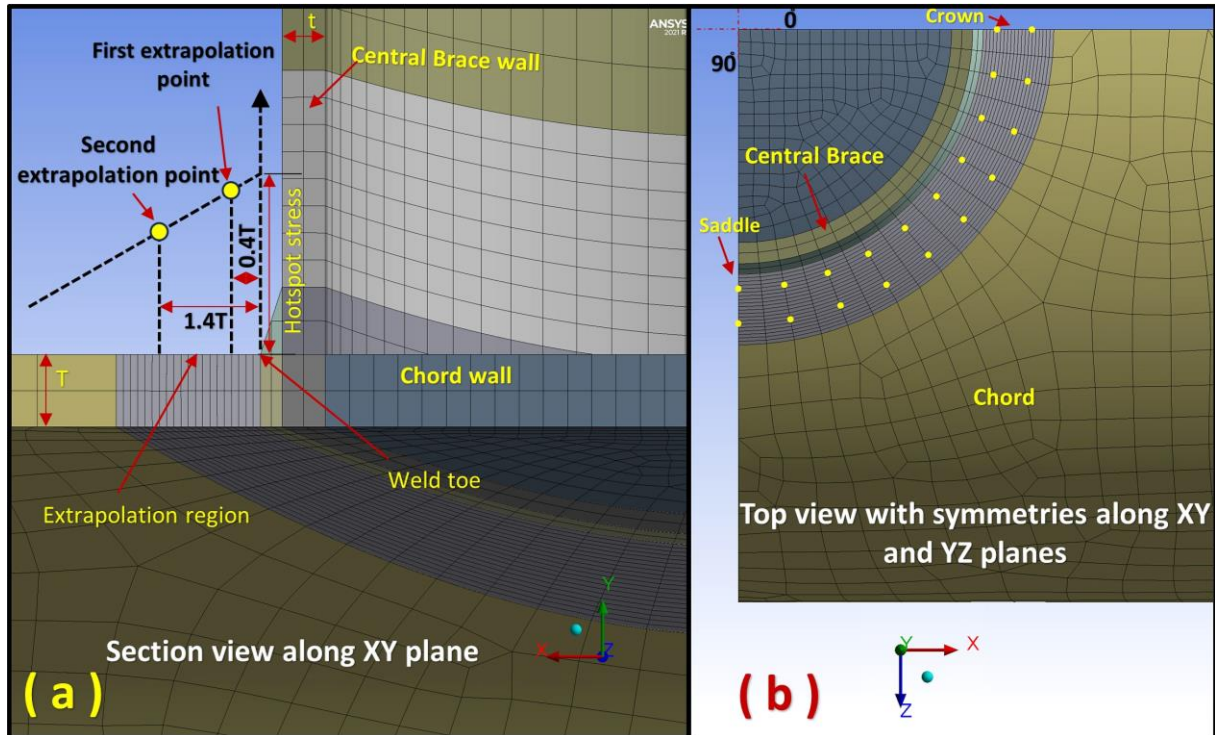


Figure 6. (a) Extrapolation procedure as established by the International Institute of Welding IIW-XV-E-(1999) [35], section view along XY-plane (b) Top view of strain gauge locations along the weld toe with symmetry along XY and YZ planes

$$SCF = \sigma_{hotspot\ stress} / \sigma_{nominal} \tag{1}$$

where

$$\sigma_{hotspot\ stress} = 1.4 \sigma_1 - 0.4 \sigma_2 \tag{2}$$

And σ_1 and σ_2 are the stresses on the first and the second extrapolation points, respectively. The first and second extrapolation points are at 0.4*T and 1.4*T from the weld toe, respectively. The nominal stress, $\sigma_{nominal}$ can be calculated as follows:

$$\sigma_{nominal} = F / \pi(r^2 - (r - t)^2) \tag{3}$$

where r and t are the radius and thickness of the brace, respectively.

The extrapolation points around the central brace, as recommended by the International Institute of Welding [35], are shown in Figure 6.

3.3. Validation of FEA Results Against Experimental Data

The FEA results were validated with the experimental results of Ahmadi et al. [4, 10, 19-24]. Figure 7 displays the stress concentration factors (SCFs) obtained through numerical analyses of recent research and the experimental and numerical findings of Ahmadi et al. [4, 10, 19-24].

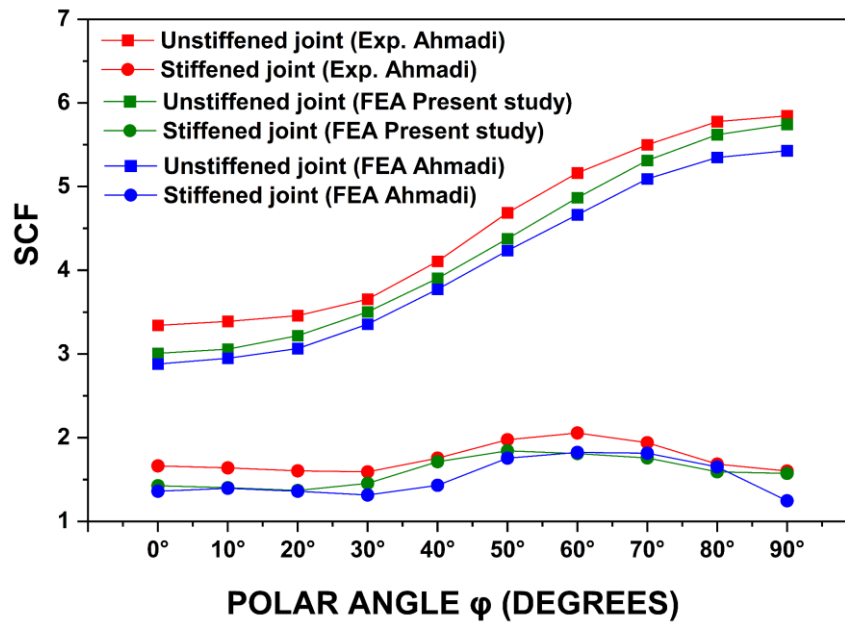


Figure 7. Validation of FEA results against experimental data [4, 10, 19-24]

Figure 7 illustrates the SCFs surrounding the weld toe of the unstiffened and stiffened KT-joints at the intersection of the central brace and the chord. A comparison has been made between experimental data and FEA results in this figure. The SCFs distribution at the weld toe of the central brace is symmetrical due to the symmetries in the joint shape and loading in the XY and YZ planes. It is sufficient to consider 1/4 of the 360° brace and chord intersection, which occurs between the crown and saddle positions (Figure 3). As shown in Figure 6, the polar angle (ϕ) along the weld path is calculated from the position of the crown, so the crown is at 0° and the saddle is at 90°.

Figure 7 shows a strong correlation between the simulation results and experimental data, proving that numerical models can reliably predict the stress concentration factors of the KT joint. The validation literature [4, 10, 19-24] had a root mean square error (RMSE) of 0.17 between the experimental results, and FEA results for unstiffened joint and stiffened joint had a root mean square error of 0.06 between experimental and FEA results. Figure 7 demonstrates that the FEA results of the current study fall within the experimental and FEA results of the scholar [10], with a root mean square error of 0.06 for unstiffened joint and 0.03 for stiffened joint.

By comparing the SCFs of unstiffened and stiffened joints, it is evident that ring-stiffeners can enhance the fatigue performance of the tubular joint by effectively decreasing the SCFs surrounding the weld toe. The SCFs of the stiffened joint are considerably more consistent than the unstiffened joint, as illustrated in Figure 7.

3.4. Scope of the Study

The scope of the study is to analyze the effect of ring parameters along with joint parameters on the stress concentration of the KT joints, to get a novel set of equations for SCF, and to get an optimized internal ring ring-reinforced KT-joint with minimum SCF.

The following dimensional and dimensionless parameters are defined with their corresponding ranges for the parametric study. The most practical ranges of parameters used in the offshore industry are given in Table 1.

Table 1. Parameters and their ranges

Sr.No.	Type of parameter	Parameter	Range	References
1	Dimensional	θ	30°, 45°, 60°	
2		β	0.4, 0.5, 0.6	
3		γ	16, 20, 24	Ahmadi et al. 2012 [4], 2013 [10], 2015 [22, 23], 2016 [21]
4		τ	0.6, 0.9	
5	Dimensionless	ζ	0.1, 0.3, 0.6	
6		λ	0.2, 0.6, 1	Xiaoyi et al. [39]
7		δ	0.1, 0.2	Lee et al. [9], Masilamani et al. [40], UK HSE [15]
8		ψ	0.4, 0.6, 0.8	Lee et al. [9], and UK HSE [15]

Efthymiou [41] has shown that to guarantee that the stresses at the brace/chord intersection are unaffected by the boundary conditions, the length of the chord should be sufficiently large (i.e., $\alpha \geq 12$). Therefore, in this investigation, a realistic value of $\alpha = 12.3$ was assigned to all the models. Chang and Dover [42] investigated the impact of brace length on SCFs and concluded that the brace length has no noticeable impact on SCFs when the α_b is above a critical value, so $\alpha_b = 15$ was selected for all simulations.

As shown in Figure 3, internal rings were positioned relative to the brace diameter at a distance of $\lambda = a.w_s$, where w_s is the distance between the outer stiffener's center in section A-A along the longitudinal axis of the chord, and "a" varies from 0.2 - 1 [39]. For the central brace, w_s is the same as the diameter of the brace, while it differs in outer inclined braces due to their angle with the chord. Three stiffeners were used under each brace.

A total of 420 simulations were performed for the parametric study, and their results are summarized in the next section.

4. Results and Discussion

After performing simulations, the effect of different joint parameters and ring parameters was investigated. The details of each section are given below. Each combination changes the stress concentration factors SCF with different magnitudes and shapes.

The SCF is significantly influenced by each dimensionless parameter (β , γ , τ , λ , δ , and ψ). The parameter definitions are presented in Figure 3. Increasing the value of β increases the diameter of the brace, leading to an increase in SCF on the chord side [10]. When γ is increased while maintaining the chord diameter constant, the chord becomes thinner, resulting in an increase in chord side SCF [25]. A greater value of τ at a constant chord thickness leads to a thicker brace, which increases the SCF [43]. The stiffener parameters (λ , δ , and ψ) decrease local bending in the chord, lowering the SCF on the chord side [16]. The stiffeners' depth had a higher influence on decreasing the SCF than their thickness [16]. Overall, the results show that the internal ring stiffened joints can significantly decrease SCF.

4.1. Effect of β on SCF Values

The parameter β represents the ratio of brace-to-chord diameter. When β increases while keeping the chord diameter constant, the brace diameter also increases. This particular sub-section investigates the influence of β on the SCFs surrounding the weld toe and explores the interaction between β and ring parameters (λ , δ , and ψ). A series of simulations were conducted to investigate the impact of β and its interactions with ring parameters (λ , δ , and ψ). In the interest of brevity, this section includes just six graphs from Figures 8-a to 8-f, although several comparison graphs were used to analyze the impact. The SCFs surrounding the weld toe for 24 models are shown in Figures 8-a, 8-c and 8-e. Figures 8-b, 8-d and 8-f illustrates the ratio between the SCF stiffened joint and the SCF unstiffened joint for the same 24 models. There are three different values of β in the six charts: 0.4, 0.5, and 0.6. The remaining joint parameters, namely γ , τ , θ , and ζ , are consistent throughout all of these 24 simulations, with $\gamma = 16.25$, $\tau = 0.6$, $\theta = 45^\circ$, and $\zeta = 0.3$. On the other hand, the ring parameters, λ , δ , and ψ , have different values in each scenario. In contrast to δ , which has values of 0.1 and 0.2, λ has values of 0.2, 0.6, and 1. Finally, ψ has values of 0.4, 0.6, and 0.8.

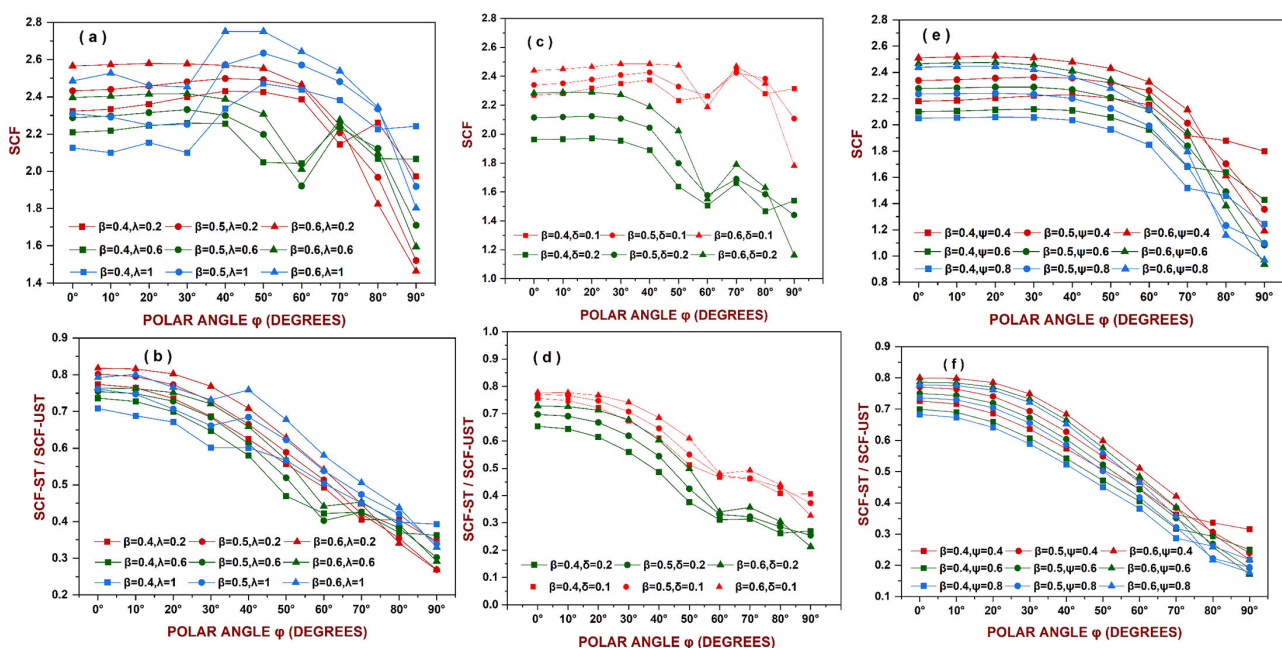


Figure 8. Effect of β on SCF values, where $\gamma = 16.25$, $\tau = 0.6$, $\theta = 45^\circ$, $\zeta = 0.3$, and for (a) and (b) $\delta = 0.1$, $\psi = 0.8$, and for (c) and (d) $\lambda = 0.6$, $\psi = 0.6$, and for (e) and (f) $\lambda = 0.2$, $\delta = 0.2$

Figure 8-a shows the SCFs surrounding the weld toe for varying values of β and its interaction with λ . By investigating the effect of β , the increase of β from 0.4 to 0.6 increases SCF at all locations around the weld and is not influenced by any other parameters [4, 10, 24]. The SCF shape around the weld toe remains the same for a given value of λ , regardless of variations in various values of β . The SCF shape around the weld toe varies with different value of λ for a constant β . By changing the values of λ , the position of the peak SCF is altered [16].

Figure 8-b illustrates the comparative ratio between the SCF stiffened joint and the SCF unstiffened joint across various values of β while considering its interaction with λ . When β increases, the ratio SCF-ST/SCF-UST also increases for the same values of λ . The saddle experiences the largest decrease in the ratio, and the crown experiences the smallest decrease.

Figure 8-c shows the SCF Surrounding the weld toe, displaying various β and its interaction with δ . When β is increased, for a constant δ , there is an increase in the SCF. The SCF Surrounding the weld toe experiences a fall when δ is increased while β is constant [4, 10, 16, 24].

Figure 8-d illustrates the comparative ratio between the SCF stiffened joint and the SCF unstiffened joint, considering various β and its interaction with δ . As β increases, for a constant δ , there is a noticeable rise in the ratio of SCF-ST to SCF-UST. The ratio decreases for increasing δ when β is constant. The saddle experiences the largest decrease in the ratio, and the crown experiences the smallest decrease.

Figure 8-e shows the SCF Surrounding the weld toe, exhibiting different values of β and its relationship with ψ . Increasing the β parameter while maintaining constant values of ψ increases the SCF Surrounding the weld toe. For a given β , the SCFs surrounding the weld toe decrease when ψ is increased SCF [16].

Figure 8-f illustrates the ratio between the SCF stiffened joint and the SCF unstiffened joint for various β while considering its interaction with ψ . The ratio of SCF-ST to SCF-UST exhibits a rise with the increase in β , for a constant ψ . The ratio decreases when the values of ψ increase for a constant β . Based on the findings shown in Figure 8-f, it can be inferred that the highest SCF drop occurs at the saddle, while the lowest SCF drop is at the crown.

By increasing the value of β by 0.1, the Peak SCF increases from 3% to 18% with different combinations of ring parameters.

4.2. Effect of γ on SCF Values

The ratio of chord diameter to twice the chord thickness is represented by the parameter γ . The chord thickness decreases with an increase in γ at a constant chord diameter. This subsection investigates the influence of γ on the SCF Surrounding the weld toe, along with the interaction between γ and ring parameters (λ , δ , and ψ). A series of simulations were conducted to investigate the impact of γ and its interactions with ring parameters (λ , δ , and ψ). In the interest of brevity, this section includes just six graphs from Figures 9-a to 9-f, although several comparison graphs were used to analyze the impact. The SCFs surrounding the weld toe for 24 models are illustrated in Figures 9-a, 9-c and 9-e. Figures 9-b, 9-d, and 9-f illustrates the ratio between the SCF stiffened joint and the SCF unstiffened joint for the same 24 models. In each of the six charts, there are three distinct values of γ , which are 16.25, 20, and 24. The values of the remaining joint parameters, namely β , τ , θ , and ζ , are consistent throughout all of these simulations, with $\beta = 0.4$, $\tau = 0.6$, $\theta = 45^\circ$, and $\zeta = 0.3$. On the other hand, the values of the ring parameters, namely λ , δ , and ψ , differ across the cases. The values for λ are 0.2, 0.6, and 1, while the values for δ are 0.1 and 0.2. Lastly, the values for ψ are 0.4, 0.6, and 0.8.

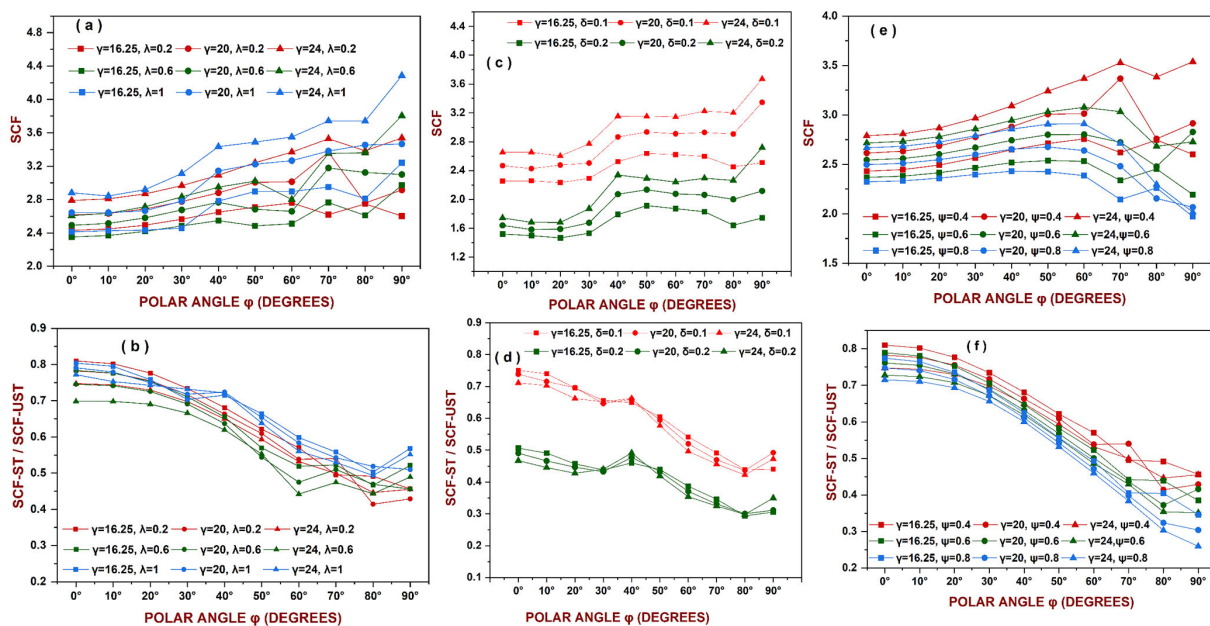


Figure 9. Effect of γ on SCF values, where $\beta=0.4$, $\tau=0.6$, $\theta=45^\circ$, $\zeta=0.3$ for (a) and (b) $\delta=0.1$, $\psi=0.4$, for (c) and (d) $\lambda=1$, $\psi=0.6$ and for (e) and (f) $\lambda=0.2$, $\delta=0.1$

Figure 9-a shows the SCF Surrounding the weld toe, displaying various values of γ and its interaction with λ . An increase of γ from 16.25 to 24 leads to a rise in SCF at all locations around the weld without being influenced by any other parameters [4, 10, 24]. The SCF shape around the weld toe varies with λ , for a constant γ [16].

Figure 9-b illustrates the ratio between the SCF stiffened joint and the SCF unstiffened joint across various γ while considering its interaction with λ . When γ increases, the ratio of SCF-ST/SCF-UST decreases for the same values of λ .

Figure 9-c shows the SCF Surrounding the weld toe, displaying various values of γ and its interaction with δ . When γ is increased while keeping δ constant, there is an increase in the SCF. When δ is increased while keeping γ constant, there is a drop in the SCF Surrounding the weld toe [4, 10, 16, 24]. The shape of SCF surrounding the weld toe remains unchanged regardless of variations in the parameter δ .

Figure 9-d illustrates the ratio between the SCF stiffened joint and the SCF unstiffened joint, considering various γ and its interaction with δ . By increasing δ while keeping γ constant, the ratio decreases.

Figure 9-e depicts the SCF Surrounding the weld toe, exhibiting different values of γ and its relationship with ψ . An increase in the γ parameter while maintaining constant values of ψ increases the SCF Surrounding the weld toe. The SCFs surrounding the weld toe decrease when the value of ψ is increased for a constant γ [16].

Figure 9-f illustrates the ratio between the SCF stiffened joint and the SCF unstiffened joint for various γ while considering its interaction with ψ . The ratio of SCF-ST to SCF-UST lessens with increasing γ for a constant ψ . The ratio decreases when ψ increases for a constant γ .

By increasing the value of γ by four from 16.25, the Peak SCF increases from 12.5% to 53.5% with different combinations of ring parameters. With a further increase in γ from 20 to 24, the Peak SCF increases from 10% to 29% with different combinations of ring parameters.

4.3. Effect of τ on SCF Values

The parameter τ represents the ratio of the thickness of the brace to the thickness of the chord; an increase in τ at constant chord thickness increases brace thickness. This sub-section investigates the influence of τ on the SCF Surrounding the weld toe. This section also examines the interaction between τ and ring parameters (λ , δ , and ψ). A series of simulations were conducted to investigate the impact of τ and its interactions with ring parameters (λ , δ , and ψ). In the interest of brevity, this section includes just six graphs from Figures 10-a to 10-f, although several comparison graphs were used to analyze the impact. The SCFs surrounding the weld toe and the ratio of SCFs stiffened joint, and the SCF unstiffened for 16 models are shown in Figure 10. In each of the six charts, there are two distinct values of τ , which are 0.6 and 0.9. The parameter τ has two values of 0.6 and 0.9, while the values of the remaining joint parameters, namely β , γ , θ , and ζ , are constant throughout all of these simulations, with $\beta = 0.4$, $\gamma = 16.25$, $\theta = 45^\circ$, and $\zeta = 0.3$. The combinations are made with three values of λ (0.2,0.6,1), two values of δ (0.1 and 0.2) and three values of ψ (0.4,0.6,0.8).

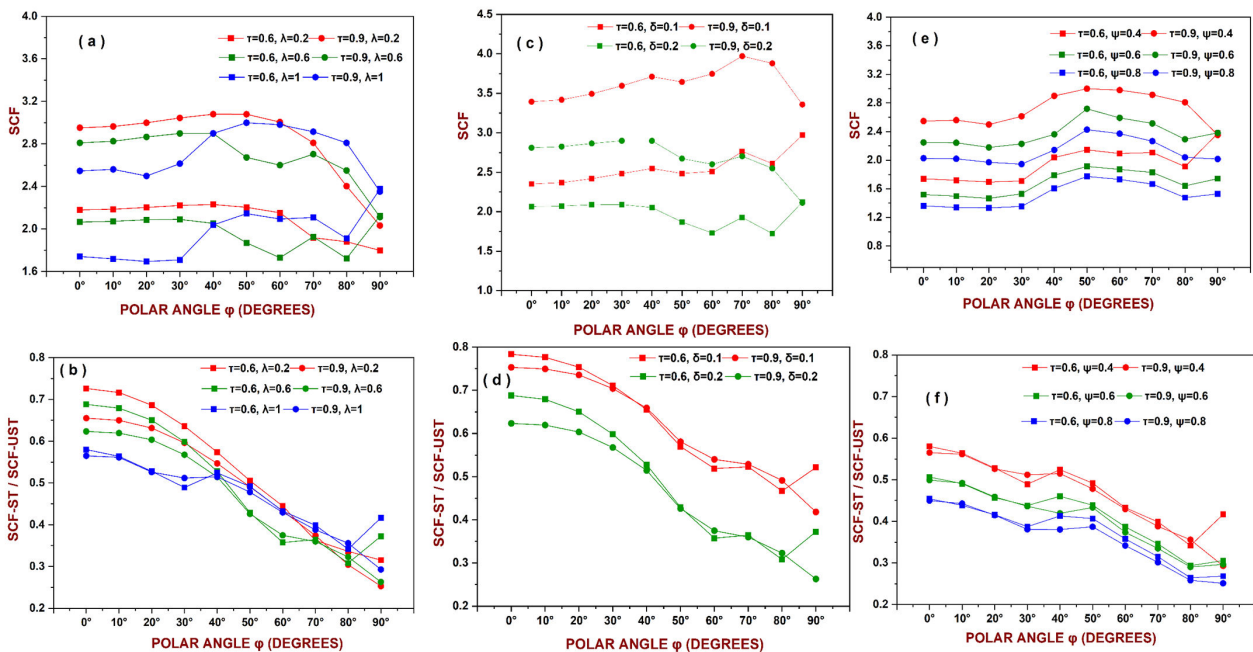


Figure 10. Effect of τ on SCF values, where $\beta = 0.4$, $\gamma = 16.25$, $\theta = 45^\circ$, $\zeta = 0.3$ for (a) and (b) $\delta = 0.2$, $\psi = 0.4$, for (c) and (d) $\lambda = 0.6$, $\psi = 0.4$ and for (e) and (f) $\lambda = 1$, $\delta = 0.2$

Figure 10-a illustrates the SCF Surrounding the weld toe for different values of τ and λ , displaying various values of τ and its interaction with λ . Increasing the τ increases SCFs surrounding the weld toe at all locations; other parameters do not influence this [4, 10, 24]. The shape of SCF changes with λ [16].

Figure 10-b illustrates the comparative ratio between the SCF stiffened joint and the SCF unstiffened joint across various τ while considering its interaction with λ .

Figure 10-c shows the SCF Surrounding the weld toe, displaying various values of τ and its interaction with δ . When τ is increased, for a constant δ , there is an increase in the SCF. When δ is increased for a constant τ , there is a decrease in the SCF Surrounding the weld toe [4, 10, 16, 24]. The SCF shape around the weld toe remains unchanged, regardless of variations in the parameter τ .

Figure 10-d illustrates the ratio between the SCF stiffened joint and the SCF unstiffened joint, considering various τ and its interaction with δ . By increasing δ , for a constant τ , the ratio decreases.

Figure 10-e illustrates the SCF Surrounding the weld toe for various τ and its relationship with ψ . The increase of the τ parameter while maintaining constant ψ increases the SCF Surrounding the weld toe. When ψ is increased, for a constant τ , the SCFs surrounding the weld toe decrease [16].

Figure 10-f illustrates the ratio between the SCF stiffened joint and the SCF unstiffened joint across various values of τ while considering its interaction with ψ . The ratio decreases when ψ increases while keeping τ constant.

By increasing the value of τ by 0.3, the Peak SCF increases from 45% to 53% with different combinations of ring parameters.

4.4. Effect of θ on SCF Values

As shown in Figure 3, the θ angle is the angle between the main chord and the outer inclined braces. This sub-section investigates the influence of θ on the SCF surrounding the weld toe, along with the interaction between θ and ring parameters (λ , δ , and ψ). A series of simulations were conducted to investigate the impact of θ and its interactions with ring parameters (λ , δ , and ψ). In the interest of brevity, this section includes just six graphs from Figures 11-a to 11-f, although several comparison graphs were used to analyze the impact.

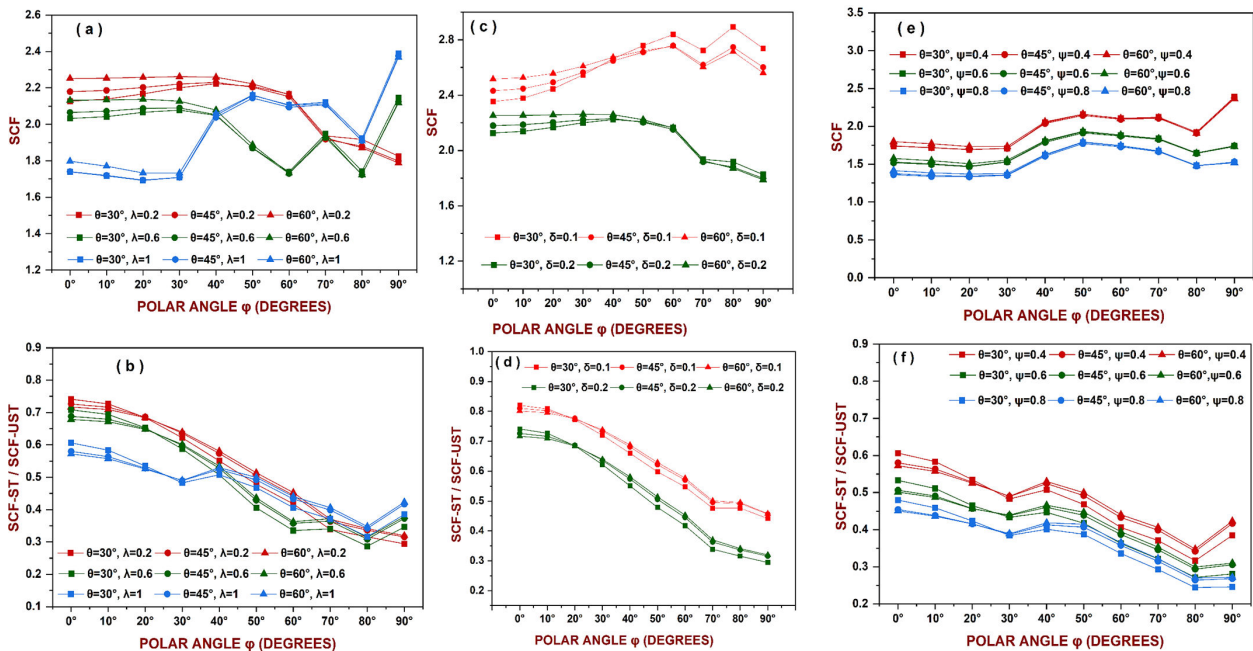


Figure 11. Effect of θ on SCF values, where $\beta = 0.4, \gamma = 16.25, \tau = 0.6, \zeta = 0.3$ for (a) and (b) $\delta = 0.2, \psi = 0.4$, for (c) and (d) $\lambda = 0.2, \psi = 0.4$ and for (e) and (f) $\lambda = 1, \delta = 0.2$

The SCFs surrounding the weld toe for 24 models are shown in Figures 11-a, 11-c and 11-e. Figures 11-b, 11-d, and 11-f illustrates the ratio between the SCF stiffened joint and the SCF unstiffened joint for the same 24 models. In each of the six charts, there are three distinct values of θ , which are $30^\circ, 45^\circ$ and 60° . The values of the remaining joint parameters, namely β, γ, τ , and ζ , are constant throughout all of these simulations, with $\beta = 0.4, \gamma = 16.25, \tau = 0.6$, and $\zeta = 0.3$. On the other hand, the values of the ring parameters, namely λ, δ , and ψ , differ across the cases. The values for λ are 0.2, 0.6, and 1, while the values for δ are 0.1 and 0.2. Lastly, the values for ψ are 0.4, 0.6, and 0.8.

Figures 11-a to 11-f shows that the angle θ does not have much impact on SCFs surrounding the weld toe and the ratio of SCF-ST/SCF-UST. The increase of δ and ψ reduces the SCFs surrounding the weld toe and the ratio of SCF-ST/SCF-UST. This conclusion is independent of all other parameters.

By increasing the value of θ by 15° , the Peak SCF increases from 0% to 4% with different combinations of ring parameters, which makes the effect of angle θ insignificant.

4.5. Effect of ζ on SCF Values

As shown in Figure 3, the parameter ζ is the distance between the central brace and the outer inclined brace. This sub-section investigates the influence of ζ on the SCF Surrounding the weld toe. This section also examines the interaction between ζ and ring parameters (λ , δ , and ψ). A series of simulations were conducted to investigate the impact of ζ and its interactions with ring parameters (λ , δ , and ψ). In the interest of brevity, this section includes just six graphs from Figures 12-a to 12-f, although several comparison graphs were used to analyze the impact. The SCFs surrounding the weld toe for 24 models are shown in Figures 12-a, 12-c and 12-e. Figures 12-b, 12-d and 12-f illustrates the ratio between the SCF stiffened joint and the SCF unstiffened joint for the same 24 models. There are three different values of ζ in all of the six charts: 0.1, 0.3, and 0.6. The remaining joint parameters, namely β , τ , θ , and γ , are consistent throughout all of these 24 simulations, with $\beta=0.4$, $\tau=0.6$, $\theta=45^\circ$, and $\gamma=16.25$. On the other hand, the ring parameters, λ , δ , and ψ , have different values in each scenario. In contrast to δ , which has values of 0.1 and 0.2, λ has values of 0.2, 0.6, and 1. Finally, ψ has values of 0.4, 0.6, and 0.8.

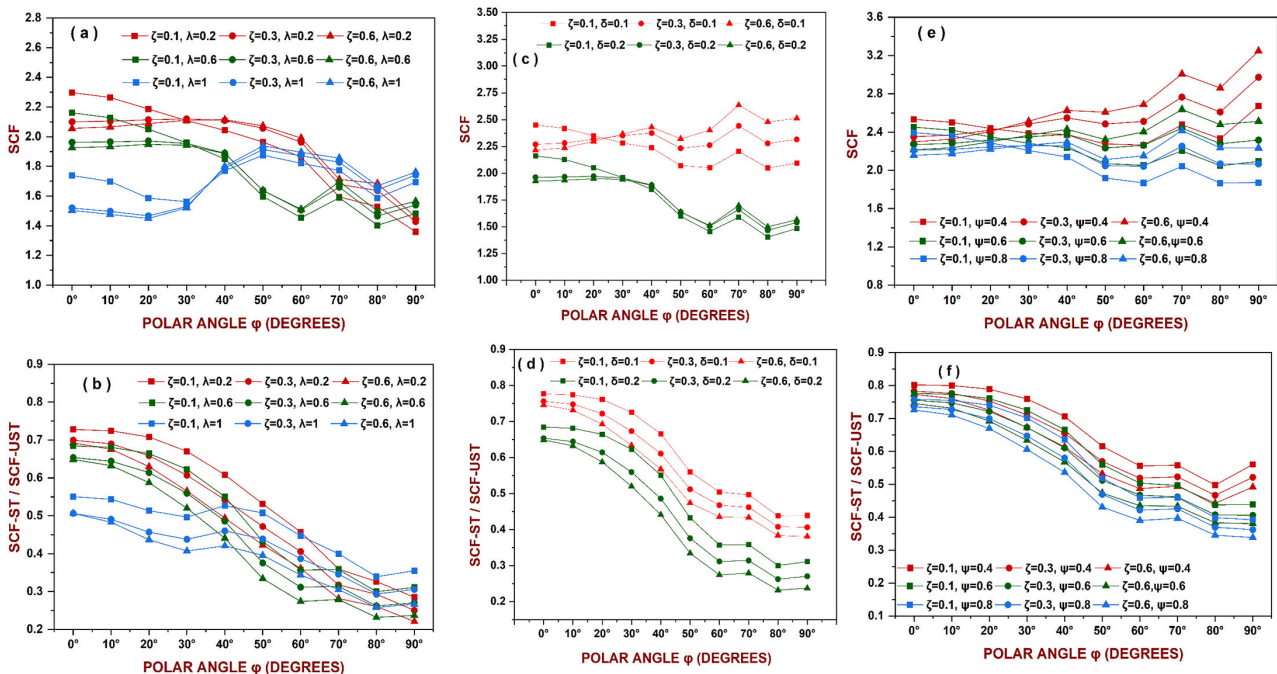


Figure 12. Effect of ζ on SCF values, where $\beta=0.4$, $\gamma=16.25$, $\tau=0.6$, $\theta=45^\circ$ for (a) and (b) $\delta=0.2$, $\psi=0.6$, for (c) and (d) $\lambda=0.6$, $\psi=0.6$ and for (e) and (f) $\lambda=0.6$, $\delta=0.1$

Figure 12-a shows the SCF Surrounding the weld toe, displaying various values of ζ and its interaction with λ . The SCF shape around the weld toe varies with varying values of λ and ζ . By changing the λ , the position of the peak SCF changes [16].

Figure 12-b illustrates the ratio between the SCF stiffened joint and the SCF unstiffened joint across various ζ while considering its interaction with λ . Figure 12-b shows that the greatest reduction in SCF caused by λ is observed at the saddle, whereas the smallest reduction in SCF is observed at the crown.

Figure 12-c shows the SCF Surrounding the weld toe, displaying various ζ and its interaction with δ . The SCF shape around the weld toe varies with different δ and ζ , by changing δ , the position of the peak SCF changes.

Figure 12-d illustrates the ratio between the SCF stiffened joint and the SCF unstiffened joint across various ζ while considering its interaction with δ . When ζ increases, the ratio of SCF-ST/SCF-UST exhibits a small decrease for the δ . Figure 12-d shows that the greatest reduction in SCF caused by δ is observed at the saddle, whereas the smallest reduction in SCF is observed at the crown.

Figure 12-e shows the SCF Surrounding the weld toe, displaying various ζ and its interaction with ψ . The SCF shape around the weld toe varies with different ψ and ζ , by changing ψ , the position of the peak SCF changes.

Figure 12-f illustrates the ratio between the SCF stiffened joint and the SCF unstiffened joint across various ζ while considering its interaction with ψ . When ζ increases, the ratio SCF-ST/SCF-UST exhibits a small decrease for the same ψ . Based on Figure 12-b, it can be observed that the largest decrease in SCF due to ψ occurs at the saddle, while the smallest decrease in SCF is seen at the crown.

By increasing the value of ζ from 0.1 to 0.3, the Peak SCF increases from 5% to 17% with different combinations of ring parameters. With further increases from 0.3 to 0.6, the Peak SCF increases from 0% to 3% with different combinations of ring parameters

5. Response Surface Methodology

RSM has been proved to give comprehensive and accurate predictions [32], their use in mathematical modeling of SCF is considered here. Seven dimensionless parameters and one-dimensional parameter, as listed in Table 1, were investigated as input components in this response surface technique. A total of 420 FEA models were developed utilizing optimal design techniques. Optimal design is an excellent substitute when the central composite and box-Behnken designs fail to align with our requirements. Within the framework of an ideal design, parameters can be evaluated in a manner free from bias and characterized by minimal variance. Unlike central composites and box-Behnken designs, an ideal design allows for determining the range of parameters using continuous and discrete alternatives. For continuous variables, their values span a range from low to high. Conversely, discrete variables possess elements that must exhibit two or more distinct levels, enabling the model to compute the response surface. The equation represented by Equation 4 is a quadratic model that is an ideal predictor. It can be employed to forecast the conditions under which reactions of significance may occur [32].

$$y = \beta_0 + \sum_{i=1}^k \beta_i x_i + \sum_{i=1}^k \beta_{ii} x_i^2 + \sum_{j=2}^k \sum_{i=1}^{j-1} \beta_{ij} x_i x_j + \epsilon \tag{4}$$

Equation 4 provides a predictive model for the SCFs over the range of 0° to 90° and the peak SCF value. Peak SCF is the highest of all ten values, ranging from SCF 0° to 90° . In this context, the symbol " β_0 " denotes a constant value. The symbol " β_i " indicates linear regression, while " β_{ii} " is associated with quadratic regression. Additionally, " β_{ij} " specifies the interconnection of the variables " x_i " and " x_j ." The symbol " ϵ " symbolizes the randomized error component. As indicated in Table 1, the variables β , γ , θ , ζ , λ , and ψ each have three levels, while τ and δ have two levels. To investigate the impact of a joint parameter, like β , from the set of joint parameters (β , ζ , τ , θ , γ) and its interaction with ring parameters (λ , δ , ψ), all other joint parameters γ , τ , θ , ζ (except β) were held constant. Subsequently, all possible combinations of the joint parameter β with the ring parameters (λ , δ , ψ) were examined using the Ansys software. Then, for combinations of γ , other joint parameters (β , τ , θ , ζ) were given a constant value. Subsequently, all possible combinations of the joint parameter γ with the ring parameters (λ , δ , ψ) were examined using the Ansys software in the same way combinations of (τ , θ , ζ) were examined in Ansys [44, 45].

5.1. ANOVA, The Analysis of Variance for Response Surface Models

The design was built utilizing the response surface derived from Equation 4 for the eleven responses that were considered (SCF at 0° to 90° and peak SCF). The quadratic model was the most suitable fit for the required outputs (SCF at 0° to 90° and peak SCF). The response surface was modeled using a complete quadratic model, resulting in 35 terms for each equation.

The ANOVA model was validated with a 95% confidence interval at a significance level of 5% [46]. The outcome of the ANOVA analysis is presented in Appendix I. A significance level of 5% was established; any values below 0.05 were considered statistically significant. The model reduction process was conducted using Minitab software, wherein only the terms with P values less than 0.05 were retained, while those with larger P values were excluded. Table 2 shows the validation parameters corresponding to each model. The output equations obtained by applying response surface methods to predict the model are provided below.

Table 2. Model validation

Model validation parameters	Responses										
	SCF 0°	SCF 10°	SCF 20°	SCF 30°	SCF 40°	SCF 50°	SCF 60°	SCF 70°	SCF 80°	SCF 90°	SCF Peak
$S \times 10^{-2}$	6.587	6.808	6.6095	5.681	4.540	3.076	7.209	6.830	9.539	1.351	1.000
R-sq	97.51%	97.47%	97.80%	98.51%	99.07%	99.68%	98.52%	98.71%	97.69%	96.45%	96.60%
R-sq(adj)	97.23%	97.20%	97.56%	98.32%	98.94%	99.62%	98.32%	98.54%	97.43%	96.08%	96.12%
R-sq(pred)	96.89%	96.86%	97.24%	98.04%	98.71%	99.54%	98.03%	98.29%	97.19%	95.63%	95.55%

Output Equations

$$\text{SCF } 0^\circ = -1.564 + 0.435 \beta + 0.05212 \gamma + 5.002 \tau + 0.003429 \theta - 1.444 \zeta + 0.902 \lambda + 6.17 \delta + 0.777 \psi + 1.443 \zeta^* \zeta - 0.1328 \lambda^* \lambda + 0.553 \beta^* \lambda + 4.60 \beta^* \delta - 0.0907 \gamma^* \delta - 10.37 \tau^* \delta - 1.073 \tau^* \psi - 6.185 \lambda^* \delta - 0.7553 \lambda^* \psi - 1.325 \delta^* \psi \quad (5)$$

$$\text{SCF } 10^\circ = -1.592 + 0.435 \beta + 0.05446 \gamma + 5.108 \tau + 0.003114 \theta - 1.143 \zeta + 1.014 \lambda + 5.56 \delta + 0.625 \psi + 1.139 \zeta^* \zeta - 0.2174 \lambda^* \lambda + 0.505 \beta^* \lambda + 4.70 \beta^* \delta - 0.1042 \gamma^* \delta - 10.34 \tau^* \delta - 1.180 \tau^* \psi - 6.428 \lambda^* \delta - 0.7320 \lambda^* \psi \quad (6)$$

$$\text{SCF } 20^\circ = -1.709 + 0.458 \beta + 0.06164 \gamma + 5.183 \tau + 0.002332 \theta + 0.136 \zeta + 1.540 \lambda + 5.61 \delta - 0.244 \psi - 0.3260 \lambda^* \lambda + 0.703 \psi^* \psi + 5.56 \beta^* \delta - 0.01302 \gamma^* \lambda - 0.0943 \gamma^* \delta - 10.75 \tau^* \delta - 1.221 \tau^* \psi - 1.755 \zeta^* \delta - 6.516 \lambda^* \delta - 0.6972 \lambda^* \psi \quad (7)$$

$$\text{SCF } 30^\circ = -2.008 - 0.358 \beta + 0.08100 \gamma + 5.685 \tau + 0.001338 \theta + 0.800 \zeta + 0.618 \lambda + 4.23 \delta + 0.833 \psi - 0.431 \zeta^* \zeta - 0.1792 \lambda^* \lambda + 0.480 \psi^* \psi + 1.107 \beta^* \lambda + 7.53 \beta^* \delta - 0.0735 \gamma^* \delta - 0.0316 \gamma^* \psi - 11.354 \tau^* \delta - 1.690 \tau^* \psi - 2.612 \zeta^* \delta - 5.488 \lambda^* \delta - 0.8319 \lambda^* \psi \quad (8)$$

$$\text{SCF } 40^\circ = -0.848 - 1.409 \beta + 0.05311 \gamma + 6.065 \tau + 1.467 \zeta - 0.913 \lambda + 3.35 \delta - 0.686 \psi - 0.944 \zeta^* \zeta + 0.9015 \lambda^* \lambda + 0.828 \psi^* \psi + 1.367 \beta^* \lambda + 8.17 \beta^* \delta + 1.136 \beta^* \psi + 0.02902 \gamma^* \lambda - 0.0706 \gamma^* \delta - 0.417 \tau^* \lambda - 11.837 \tau^* \delta - 1.843 \tau^* \psi - 3.483 \zeta^* \delta - 4.369 \lambda^* \delta - 0.7530 \lambda^* \psi \quad (9)$$

$$\text{SCF } 50^\circ = -0.893 - 0.804 \beta + 0.09309 \gamma + 5.909 \tau - 0.00852 \theta + 1.935 \zeta - 2.1779 \lambda + 3.549 \delta - 1.003 \psi + 0.000071 \theta^* \theta - 0.927 \zeta^* \zeta + 2.2465 \lambda^* \lambda + 0.865 \psi^* \psi + 0.479 \beta^* \lambda + 5.999 \beta^* \delta + 1.332 \beta^* \psi - 0.1217 \gamma^* \delta - 0.02215 \gamma^* \psi + 0.1072 \tau^* \lambda - 12.837 \tau^* \delta - 1.458 \tau^* \psi + 0.01335 \theta^* \delta - 4.365 \zeta^* \delta - 0.413 \zeta^* \psi - 3.529 \lambda^* \delta - 0.4071 \lambda^* \psi + 1.059 \delta^* \psi \quad (10)$$

$$\text{SCF } 60^\circ = -0.996 - 0.182 \beta + 0.0907 \gamma + 6.350 \tau - 0.001541 \theta + 2.279 \zeta - 2.946 \lambda + 3.24 \delta - 0.434 \psi - 1.047 \zeta^* \zeta + 2.9679 \lambda^* \lambda + 1.145 \psi^* \psi + 5.23 \beta^* \delta - 0.1483 \gamma^* \delta - 0.0301 \gamma^* \psi - 12.84 \tau^* \delta - 2.434 \tau^* \psi - 5.433 \zeta^* \delta - 0.439 \zeta^* \psi - 2.767 \lambda^* \delta - 0.290 \lambda^* \psi + 2.067 \delta^* \psi \quad (11)$$

$$\text{SCF } 70^\circ = -1.807 - 1.095 \beta + 0.1614 \gamma + 6.367 \tau - 0.001827 \theta + 2.234 \zeta - 0.269 \lambda + 2.96 \delta - 1.294 \psi - 1.111 \zeta^* \zeta + 0.8716 \lambda^* \lambda + 1.601 \psi^* \psi + 5.44 \beta^* \delta + 1.315 \beta^* \psi - 0.01619 \gamma^* \lambda - 0.1813 \gamma^* \delta - 0.0865 \gamma^* \psi - 13.96 \tau^* \delta - 2.317 \tau^* \psi - 6.100 \zeta^* \delta - 1.782 \lambda^* \delta + 2.806 \delta^* \psi \quad (12)$$

$$\text{SCF } 80^\circ = -0.610 + 0.1230 \gamma + 5.421 \tau - 0.00808 \theta + 2.156 \zeta - 2.080 \lambda - 0.30 \delta - 0.036 \psi - 0.760 \zeta^* \zeta + 0.6197 \lambda^* \lambda + 1.578 \psi^* \psi + 0.04252 \gamma^* \lambda - 0.1354 \gamma^* \psi + 0.877 \tau^* \lambda - 12.91 \tau^* \delta - 2.351 \tau^* \psi + 0.00729 \theta^* \lambda - 6.89 \zeta^* \delta + 3.231 \delta^* \psi \quad (13)$$

$$\text{SCF } 90^\circ = -2.04 - 6.896 \beta + 0.6110 \gamma + 2.088 \tau + 1.572 \zeta + 0.463 \lambda - 2.43 \delta - 2.259 \psi - 0.01030 \gamma^* \gamma + 7.39 \beta^* \delta + 4.98 \beta^* \psi + 0.0283 \gamma^* \lambda - 0.2250 \gamma^* \psi - 13.50 \tau^* \delta + 3.205 \tau^* \psi - 6.92 \zeta^* \delta - 0.749 \lambda^* \psi + 3.13 \delta^* \psi \quad (14)$$

$$\text{SCF Peak} = -2.168 - 2.991 \beta + 0.3431 \gamma + 4.741 \tau + 1.671 \zeta - 0.420 \lambda + 3.24 \delta - 2.432 \psi - 0.00443 \gamma^* \gamma + 0.7063 \lambda^* \lambda + 1.729 \psi^* \psi + 11.77 \beta^* \delta + 3.290 \beta^* \psi + 0.04473 \gamma^* \lambda - 0.3025 \gamma^* \delta - 0.1173 \gamma^* \psi - 12.23 \tau^* \delta + 0.546 \zeta^* \lambda - 7.10 \zeta^* \delta - 1.199 \zeta^* \psi - 4.307 \lambda^* \delta - 1.121 \lambda^* \psi + 5.428 \delta^* \psi \quad (15)$$

The coefficient of determination, also known as R^2 , is employed to assess the accuracy of the model's predictions. This statement elucidates the degree to which the provided data and model align. The variable R^2 is quantified on a scale from zero to 100 percent. The calculated values of R^2 in the generated model are presented in Table 2, exhibiting a range of 96.45 to 99.07. High R^2 values serve as a trustworthy indication of the robustness of the built model.

The standard error of the estimate, symbolized as S , quantifies the extent of fluctuation between the predicted and actual values. A decreased S value indicates a heightened coherence between the predicted results and the empirical data. The values of S in the constructed model are provided in Table 2, spanning from 0.0100053 to 0.0720973. A greater value of the adjusted R-squared ($R\text{-sq}(\text{adj})$) indicates a more optimal balance between the model's fit quality and its simplicity, which is essential for assuring reliable predictions within the optimization framework. The adjusted R-squared values for the derived model are presented in Table 2, ranging from 96.12 to 99.62. The assessment of R-squared prediction ($R\text{-sq}(\text{pred})$) is of great significance in the field of response surface methodology. It serves as an indicator for evaluating the model's ability to anticipate new and unseen data points effectively. A higher value of R-squared (pred) indicates better prediction accuracy, therefore validating the reliability of the response surface model beyond the available data used for model estimation. The values of R-squared (pred) in this established model are presented in Table 2, exhibiting a range of 95.55 to 99.54.

The evaluation of model accuracy is commonly performed using two essential diagnostic tools: actual vs. predicted plots and residual plots. Two distinct types of plots may be observed in the response models depicted in Figures 13 and 14, respectively. For a model to be deemed a satisfactory fit, the data points in a plot illustrating SCF extracted from FEA and predicted by proposed equations must be aligned as closely as possible with the corresponding fitted line. The data points in this specific model instance are diagonally aligned with the fitted line, indicating a strong correlation between the projected values and the SCF derived from FEA. This indicator serves as a reliable measure of the accuracy of the response models.

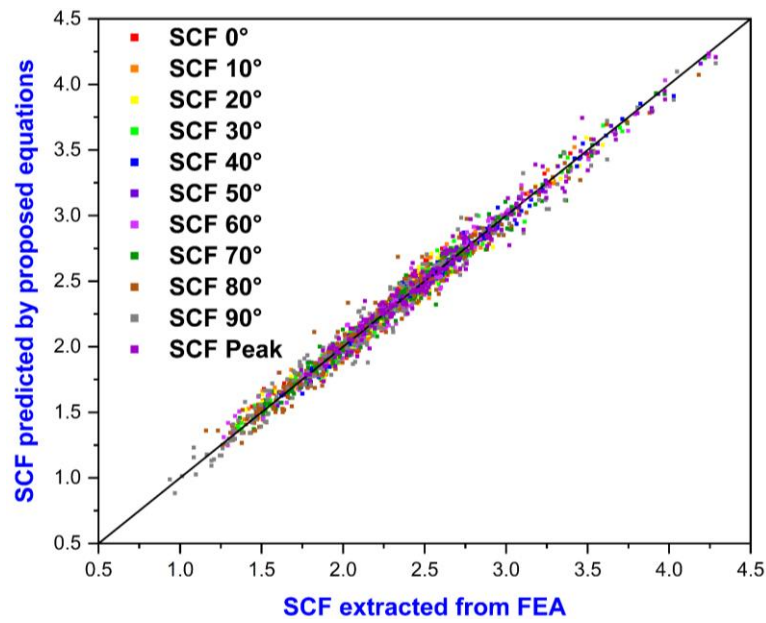


Figure 13. Comparison of SCF extracted from FEA and predicted by proposed Equations

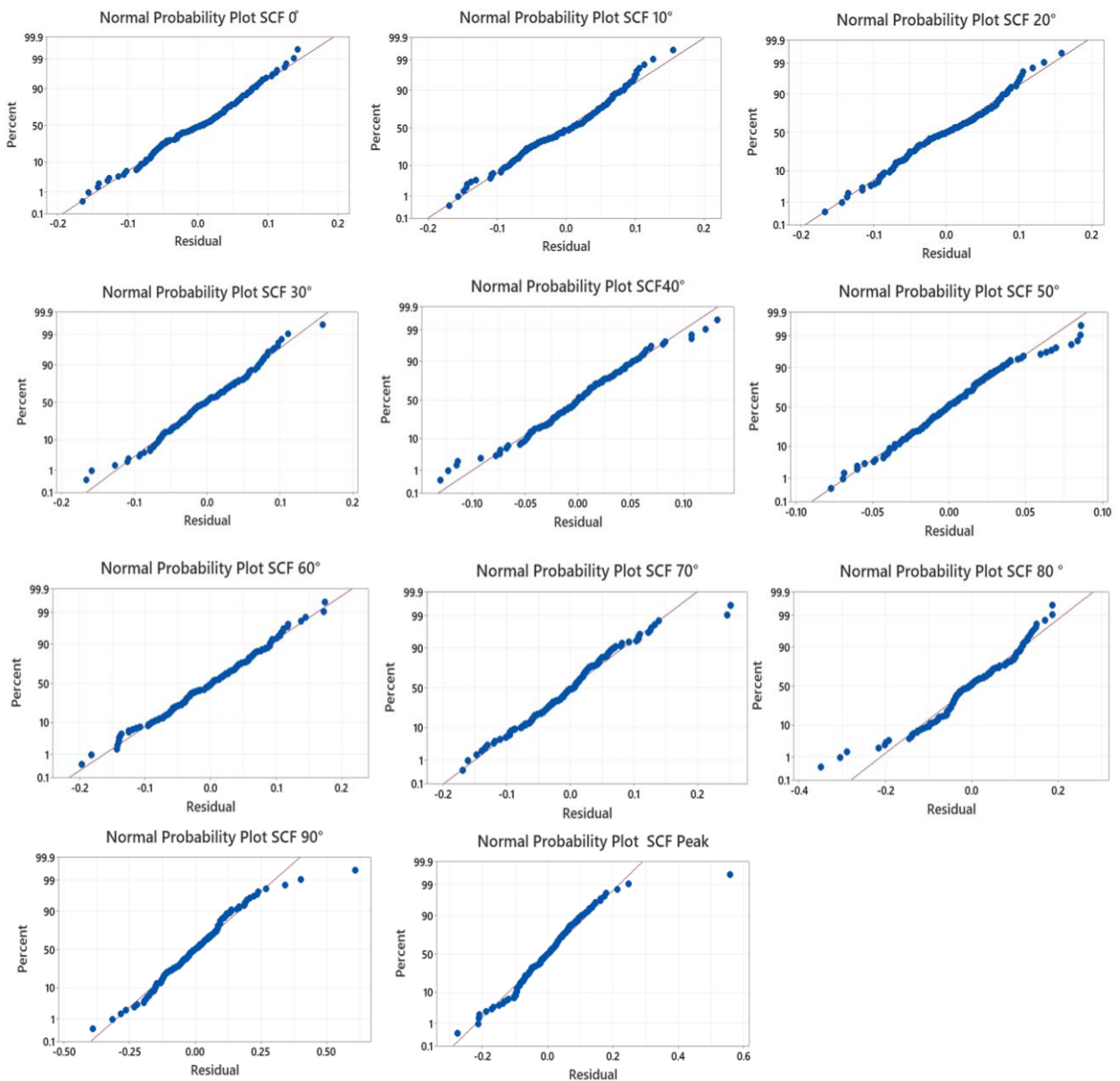


Figure 14. Normal probability plots for SCF 0 to 90 and SCF Peak

Additionally, Figure 14 offers a graphical depiction of residuals' normal plots. This observation serves as evidence for the notion that error components exhibit uniform distribution, as it illustrates the linearity of the points along the diagonal. One of the key attributes that distinguishes a dependable model is its defining trait. This phenomenon can be attributed to the observation that if the residuals conform to a normal distribution, approximately 95% of them are expected to lie within the range of -2 to +2 to satisfy the criteria for a normal distribution [32]. In this analysis, it is evident that all residual plots exhibit conformity, hence indicating the models' predictive accuracy (see Figure 14).

5.2. Multi-Objective Optimization

Multi-objective optimization involves simultaneously optimizing multiple objectives that may conflict with each other in a given problem. Multi-objective optimization, sometimes referred to as multi-response optimization, is a technique used to identify the optimal values for variables in order to maximize several responses simultaneously. A significant proportion of optimization issues encountered in practical scenarios necessitate the identification of several optimal solutions while considering numerous conflicting objectives [32]. Hence, based on the available evidence, this particular method emerges as the more favorable choice. The independent variable of the model underwent optimization in order to enhance its effectiveness. The optimization process outcome for each individual answer is ultimately determined by the desirability value, which is represented by the interval $0 \leq d_j \leq 1$. The value in question exhibits a range between 0 and 1. By increasing the value of the d_j variable, the resulting outcome can be rendered more advantageous, expressed as a percentage. The geometric mean of each answer's desirability is employed during the multi-objective optimization method [32]. This makes it possible to determine the desirability value of the composite response, as indicated by Equation 16.

$$D = (D_1^{r1} \times D_2^{r2} \times D_3^{r3} \dots \times D_n^{rm})^{1/n} \tag{16}$$

The variable "n" denotes the overall count of responses taken into account during the optimization process. The term "ri" denotes the magnitude of significance attributed to individual functions, with a range of values from 1 (indicating little relevance) to 5 (representing utmost essentiality). In the present study, the identical procedure was employed, and a limit of desirability was established within the range of 0 to 1. When the desirability value reaches 1, it indicates a more positive outcome for the model and increases the reliability of the optimized results in estimating the dependent variable. The objective of the fatigue design is to minimize the stress concentration factors. SCF optimization aims to minimize the peak SCF and SCF at 0° to 90°. Based on the optimization of the outcomes, the optimal dimensionless and dimensional parameters are as follows: $\lambda=0.951515$, $\delta=0.2$, $\psi=0.8$, $\zeta=0.31$, $\theta=45.15^\circ$, $\tau=0.60$, $\gamma=16.25$, and $\beta=0.40$. The model's desirability is 0.9248, indicating highly pertinent outcomes, which indicates that the optimization strategy produced highly desirable outcomes.

As demonstrated in Table 3, an FEA verification was performed to determine the discrepancy between the obtained numerical values and the predicted response values resulting from the optimization technique. The model was developed based on the ideal parameters suggested by multi-objective optimization. The percentage error is calculated to compare optimized and numerical values. The data clearly shows that the percentage error for all responses is less than 6%. The close correlation between the optimized outcomes and the findings obtained from finite element analysis demonstrates significant accuracy.

Table 3. Results of FEA validation of the optimized value.

Response	Predicted	FEA	Error (%)
SCF 0°	1.42	1.50	-5.1
SCF 10°	1.42	1.47	-3.8
SCF 20°	1.40	1.40	0.0
SCF 30°	1.42	1.36	4.2
SCF 40°	1.62	1.54	5.2
SCF 50°	1.67	1.74	-3.9
SCF 60°	1.67	1.72	-3.2
SCF 70°	1.65	1.65	0
SCF 80°	1.52	1.47	3.6
SCF 90°	1.47	1.39	5.7
SCF Peak	1.67	1.74	-3.9

6. Conclusions

After performing 420 FEA simulations, the following points were observed.

- (a) The outcome of the parametric study is summarized below.
- By increasing the value of β by 0.1, the Peak SCF increases from 3% to 18% with different combinations of ring parameters.
 - By increasing the value of γ by four from 16.25, the Peak SCF increases from 12.5% to 53.5% with different combinations of ring parameters. With a further increase from 20 to 24, the Peak SCF increases from 10% to 29% with different combinations of ring parameters.
 - By increasing the value of τ by 0.3, the Peak SCF increases from 45% to 53% with different combinations of ring parameters.
 - By increasing the value of θ by 15°, the Peak SCF increases from 0% to 4% with different combinations of ring parameters. This little increase indicates that this parameter does not have much impact on the stress concentration factors.
 - By increasing the value of ζ from 0.1 to 0.3, the Peak SCF increases from 5% to 17% with different combinations of ring parameters. With a further increase from 0.3 to 0.6, the Peak SCF increases from 0% to 3% with different combinations of ring parameters.
 - The stiffeners decrease local bending in the chord, which decreases the SCF on the chord side.
 - Stiffeners' height had a higher influence on decreasing the SCF than their thickness.
- (b) The response surface methodology for internally reinforced KT-joint stress concentration factor optimization under compressive load was presented in this study. The response surface model and suggested mathematical formulas provide a high degree of precision in predicting the stress concentration variables. Since different combinations of rings can result in varied stress concentration factors and shapes, all of the ring characteristics were used. Engineers in practice, can use these equations to accurately forecast the SCF at ten locations and the SCF peak value within seconds. The SCFs and the nominal load can be used for quick calculations of the hotspot stress. The aforementioned equations serve to reduce potential failure resulting from fatigue load by precisely determining the hotspot stress employed in the S-N curves for the fatigue life of tubular joints.
- (c) The optimal outcome with the lowest stress concentration parameters could extend the fatigue life of offshore constructions.

7. Nomenclature

D	Chord diameter	d	Brace diameter
T	Chord thickness	t	Brace thickness
θ	Angle between the outer inclined brace and the chord	L	Chord length
H	Height of brace	g	Gap between central brace and outer inclined brace
h_s	Height of the stiffener	t_s	Thickness of the stiffener
w_s	Distance between outer stiffener's center	β	Ratio of the diameter of brace and chord
γ	Ratio of chord's diameter and twice chord's thickness	τ	Ratio of brace thickness to chord thickness
ζ	Ratio of "gap between central and outer inclined brace" and diameter of the chord	α	Ratio of twice the length of the chord to the diameter of the chord
α_b	Ratio of twice the length of brace to the diameter of the brace	h_s	Difference between outer and inner diameters of internal rings
δ	Ratio of "difference between outer and inner diameters of internal rings" and diameter of the chord	ψ	Ratio of the thickness of rings to the thickness of the chord
λ	Product of the width of outer stiffener and spacing ratio "a."	SCF	Stress concentration factors
IRS	Internally ring stiffened joints	SCF peak	Maximum stress concentration factors
HSS	Hotspot stress	IPB	In-plane bending
OPB	Out-of-plane bending	AWS	The American welding society
IIW	International institute of welding	RSM	Response surface methodology
ANOVA	Analysis of variance	P-value	Significance level
R^2	Coefficient of determination	S	Standard error of estimate
$R^2(\text{adj})$	Optimal balance between model, fit and quality	$R^2(\text{Predicted})$	Model's ability to assess new data
Dj value	Desirability value	β^o	Constant in quadratic predictive model
β_i	Linear regression coefficient	β_{ii}	Quadratic regression coefficient
β_{ij}	Coefficient for coupling terms	ϵ	Random error component
RMSE	Root Mean Square Error	FEA	Finite Element Analysis
x_i and x_j	Input variables	S-N curve	Stress-number of cycles to failure curve

8. Declarations

8.1. Author Contributions

Conceptualization, A.R. and S.K.; methodology, A.R. and S.K.; software, A.R. and M.I.; validation, A.R.; formal analysis, A.R.; investigation, A.R.; resources, S.K.; data curation, S.K. and A.R.; writing—original draft preparation, A.R.; writing—review and editing, A.R. and M.O.; visualization, A.R. and M.I; supervision, S.K., V.P., and M.O.; project administration, S.K. and V.P.; funding acquisition, S.K. All authors have read and agreed to the published version of the manuscript.

8.2. Data Availability Statement

The data presented in this study are available in the article.

8.3. Funding

This research received funding from Yayasan Universiti Teknologi PETRONAS under grant No. 015LC0-443.

8.4. Conflicts of Interest

The authors declare no conflict of interest.

9. References

- [1] Ahmadi, H., & Imani, H. (2022). SCFs in offshore two-planar tubular TT-joints reinforced with internal ring stiffeners. *Ocean Systems Engineering*, 12(1), 1–22. doi:10.12989/ose.2022.12.1.001.
- [2] Wardenier, J., Kurobane, Y., Packer, J. A., Van der Vegte, G. J., & Zhao, X. L. (2008). Design guide for circular hollow section (CHS) joints under predominantly static loading. CIDECT, Geneva, Switzerland.
- [3] Iqbal, M., Karuppanan, S., Perumal, V., Ovinis, M., & Rasul, A. (2023). Rehabilitation Techniques for Offshore Tubular Joints. *Journal of Marine Science and Engineering*, 11(2), 461. doi:10.3390/jmse11020461.
- [4] Ahmadi, H., Ali Lotfollahi-Yaghin, M., Yong-Bo, S., & Aminfar, M. H. (2012). Parametric study and formulation of outer-brace geometric stress concentration factors in internally ring-stiffened tubular KT-joints of offshore structures. *Applied Ocean Research*, 38, 74–91. doi:10.1016/j.apor.2012.07.004.
- [5] Zavvar, E., Hectors, K., & De Waele, W. (2021). Stress concentration factors of multi-planar tubular KT-joints subjected to in-plane bending moments. *Marine Structures*, 78. doi:10.1016/j.marstruc.2021.103000.
- [6] Iqbal, M., Karuppanan, S., Perumal, V., Ovinis, M., & Nouman, H. (2023). Empirical modeling of stress concentration factors using finite element analysis and artificial neural networks for the fatigue design of tubular KT-joints under combined loading. *Fatigue & Fracture of Engineering Materials & Structures*, 46(11), 4333–4349. doi:10.1111/ffe.14122.
- [7] Ahmadi, H., Lotfollahi-Yaghin, M. A., & Aminfar, M. H. (2012). The development of fatigue design formulas for the outer brace SCFs in offshore three-planar tubular KT-joints. *Thin-Walled Structures*, 58, 67–78. doi:10.1016/j.tws.2012.04.011.
- [8] Dehghani, A., & Aslani, F. (2019). A review on defects in steel offshore structures and developed strengthening techniques. *Structures*, 20, 635–657. doi:10.1016/j.istruc.2019.06.002.
- [9] Lee, M. M. K., & Llewelyn-Parry, A. (1999). Strength of ring-stiffened tubular T-joints in offshore structures: A numerical parametric study. *Journal of Constructional Steel Research*, 51(3), 239–264. doi:10.1016/S0143-974X(99)00027-9.
- [10] Ahmadi, H., Lotfollahi-yaghin, M. A., & Yong-bo, S. (2013). Experimental and Numerical Investigation of Geometric SCFs in Internally Ring-Stiffened Tubular KT-Joints of Offshore Structures. *Journal of the Persian Gulf*, 43(1), 7-8.
- [11] Pan, Z., Wu, G., Si, F., Shang, J., Zhou, H., Li, Q., & Zhou, T. (2022). Parametric study on SCF distribution along the weld toe of internally ring-stiffened two-planar tubular KK joints under axial loading. *Ocean Engineering*, 248, 110826. doi:10.1016/j.oceaneng.2022.110826.
- [12] Krishna, G. C. S., & Nallayarasu, S. (2022). Experimental and numerical investigation on stress concentration at brace-ring intersection (BRI) of internally ring stiffened tubular T-joints. *Applied Ocean Research*, 126, 103288. doi:10.1016/j.apor.2022.103288.
- [13] Kuang, J. G., Potvin, A. B., & Leick, R. D. (1975). Stress Concentration in Tubular Joints. Proceedings of the Offshore Technology Conference, Paper OTC 2205, Houston, United States.
- [14] HSE OTH 354. (1997). Stress Concentration Factors for Simple Tubular Joints: Assessment of Existing and Development of New Parametric Formulate. UK Health and Safety Executive (HSE), Bootle, United Kingdom.

- [15] Offshore, W. (1991). In-service database for ring-stiffened tubular joints. Report WOL, 35, 91.
- [16] Nwosu, D. I., Swamidass, A. S. J., & Munaswamy, K. (1995). Numerical stress analysis of internal ring-stiffened tubular T-joints. *Journal of Offshore Mechanics and Arctic Engineering*, 117(2), 113–125. doi:10.1115/1.2827061.
- [17] Azari Dodaran, N., Ahmadi, H., & Lotfollahi-Yaghin, M. A. (2018). Static strength of axially loaded tubular KT-joints at elevated temperatures: Study of geometrical effects and parametric formulation. *Marine Structures*, 61, 282–308. doi:10.1016/j.marstruc.2018.06.009.
- [18] Lotfollahi-Yaghin, M. A., & Ahmadi, H. (2010). Effect of geometrical parameters on SCF distribution along the weld toe of tubular KT-joints under balanced axial loads. *International Journal of Fatigue*, 32(4), 703–719. doi:10.1016/j.ijfatigue.2009.10.008.
- [19] Ahmadi, H. (2016). A probability distribution model for SCFs in internally ring-stiffened tubular KT-joints of offshore structures subjected to out-of-plane bending loads. *Ocean Engineering*, 116, 184–199. doi:10.1016/j.oceaneng.2016.02.037.
- [20] Ahmadi, H., Mohammadi, A. H., & Yeganeh, A. (2015). Probability density functions of SCFs in internally ring-stiffened tubular KT-joints of offshore structures subjected to axial loading. *Thin-Walled Structures*, 94, 485–499. doi:10.1016/j.tws.2015.05.012.
- [21] Ahmadi, H., Yeganeh, A., Mohammadi, A. H., & Zavvar, E. (2016). Probabilistic analysis of stress concentration factors in tubular KT-joints reinforced with internal ring stiffeners under in-plane bending loads. *Thin-Walled Structures*, 99, 58–75. doi:10.1016/j.tws.2015.11.010.
- [22] Ahmadi, H., & Zavvar, E. (2015). Stress concentration factors induced by out-of-plane bending loads in ring-stiffened tubular KT-joints of jacket structures. *Thin-Walled Structures*, 91, 82–95. doi:10.1016/j.tws.2015.02.011.
- [23] Ahmadi, H., & Lotfollahi-Yaghin, M. A. (2015). Stress concentration due to in-plane bending (IPB) loads in ring-stiffened tubular KT-joints of offshore structures: Parametric study and design formulation. *Applied Ocean Research*, 51, 54–66. doi:10.1016/j.apor.2015.02.009.
- [24] Ahmadi, H., Lotfollahi-Yaghin, M. A., & Yong-Bo, S. (2013). Chord-side SCF distribution of central brace in internally ring-stiffened tubular KT-joints: A geometrically parametric study. *Thin-Walled Structures*, 70, 93–105. doi:10.1016/j.tws.2013.04.011.
- [25] Sadat Hosseini, A., Zavvar, E., & Ahmadi, H. (2021). Stress concentration factors in FRP-strengthened steel tubular KT-joints. *Applied Ocean Research*, 108, 102525. doi:10.1016/j.apor.2021.102525.
- [26] Iqbal, M., Karuppanan, S., Perumal, V., Ovinis, M., & Rasul, A. (2023). Numerical Investigation of Crack Mitigation in Tubular KT-Joints Using Composite Reinforcement. *The 4th International Electronic Conference on Applied Sciences*. doi:10.3390/asec2023-16290.
- [27] Aidibi, A., Babamohammadi, S., Fatnuzzi, N., Correia, J. A. F. O., & Manuel, L. (2021). Stress Concentration Factor Evaluation of Offshore Tubular KT Joints Based on Analytical and Numerical Solutions: Comparative Study. *Practice Periodical on Structural Design and Construction*, 26(4), 1–10. doi:10.1061/(asce)sc.1943-5576.0000622.
- [28] Iqbal, M., Karuppanan, S., Perumal, V., Ovinis, M., & Hina, A. (2023). An Artificial Neural Network Model for the Stress Concentration Factors in KT-Joints Subjected to Axial Compressive Load. *Materials Science Forum*, 1103, 163–175. doi:10.4028/p-ypo50i.
- [29] American Petroleum Institute (API). (2007). *Recommended Practice for Planning, Designing and Constructing Fixed Offshore Platforms — Working Stress Design*. American Petroleum Institute (API), Washington, United States.
- [30] DNV-RP-C203 (2016). *Fatigue Design of Offshore Steel Structures*. Det Norske Veritas, Oslo, Norway.
- [31] Sadat Hosseini, A., Bahaari, M. R., & Lesani, M. (2019). Parametric Study of FRP Strengthening on Stress Concentration Factors in an Offshore Tubular T-Joint Subjected to In-Plane and Out-of-Plane Bending Moments. *International Journal of Steel Structures*, 19(6), 1755–1766. doi:10.1007/s13296-019-00244-0.
- [32] Khan, M. B., Iqbal Khan, M., Shafiq, N., Abbas, Y. M., Imran, M., Fares, G., & Khatib, J. M. (2023). Enhancing the mechanical and environmental performance of engineered cementitious composite with metakaolin, silica fume, and graphene nanoplatelets. *Construction and Building Materials*, 404, 133187. doi:10.1016/j.conbuildmat.2023.133187.
- [33] N'Diaye, A., Hariri, S., Pluvinage, G., & Azari, Z. (2007). Stress concentration factor analysis for notched welded tubular T-joints. *International Journal of Fatigue*, 29(8), 1554–1570. doi:10.1016/j.ijfatigue.2006.10.030.
- [34] AWS D1.1/D1.1M. (2020). *Structural Welding Code-Steel*. American Welding Society (AWS) D1 Committee on Structural Welding, American National Standards Institute, Washington, United States.
- [35] IIW-XV-E. (1999). *Recommended fatigue design procedure for welded hollow section joints*. International Institute of Welding, Genoa, Italy.

- [36] Hosseini, A. S., Bahaari, M. R., & Lesani, M. (2020). SCF distribution in FRP-strengthened tubular T-joints under brace axial loading. *Scientia Iranica*, 27(3), 1113–1129. doi:10.24200/SCI.2018.5471.1293.
- [37] Sadat Hosseini, A., Bahaari, M. R., & Lesani, M. (2019). Stress concentration factors in FRP-strengthened offshore steel tubular T-joints under various brace loadings. *Structures*, 20, 779–793. doi:10.1016/j.istruc.2019.07.004.
- [38] Ahmadi, H., Lotfollahi-Yaghin, M. A., & Aminfar, M. H. (2011). Geometrical effect on SCF distribution in uni-planar tubular DKT-joints under axial loads. *Journal of Constructional Steel Research*, 67(8), 1282–1291. doi:10.1016/j.jcsr.2011.03.011.
- [39] Lan, X., Wang, F., Ning, C., Xu, X., Pan, X., & Luo, Z. (2016). Strength of internally ring-stiffened tubular DT-joints subjected to brace axial loading. *Journal of Constructional Steel Research*, 125, 88–94. doi:10.1016/j.jcsr.2016.06.012.
- [40] Masilamani, R., & Nallayarasu, S. (2021). Experimental and numerical investigation of ultimate strength of ring-stiffened tubular T-joints under axial compression. *Applied Ocean Research*, 109, 102576. doi:10.1016/j.apor.2021.102576.
- [41] Efthymiou, M. (1988). Development of SCF formulae and generalized influence functions for use in fatigue analysis. OTJ 88. *Recent Developments in Tubular Joints Technology*, Surrey, United Kingdom.
- [42] Chang, E., & Dover, W. D. (1999). Parametric equations to predict stress distributions along the intersection of tubular X and DT-joints. *International Journal of Fatigue*, 21(6), 619–635. doi:10.1016/S0142-1123(99)00018-3.
- [43] Bao, S., Wang, W., Chai, Y. H., & Li, X. (2020). Hot spot stress parametric equations for three-planar tubular Y-joints subject to in-plane bending moment. *Thin-Walled Structures*, 149, 106648. doi:10.1016/j.tws.2020.106648.
- [44] Nassiraei, H., Mojtahedi, A., & Lotfollahi-Yaghin, M. A. (2018). Static strength of X-joints reinforced with collar plates subjected to brace tensile loading. *Ocean Engineering*, 161, 227–241. doi:10.1016/j.oceaneng.2018.05.017.
- [45] Nassiraei, H. (2020). Local joint flexibility of CHS T/Y-connections strengthened with collar plate under in-plane bending load: Parametric study of geometrical effects and design formulation. *Ocean Engineering*, 202, 107054. doi:10.1016/j.oceaneng.2020.107054.
- [46] Karim, M. A., Abdullah, M. Z., Waqar, A., Deifalla, A. F., Ragab, A. E., & Khan, M. (2023). Analysis of the mechanical properties of the single layered braid reinforced thermoplastic pipe (BRTP) for oil & gas industries. *Results in Engineering*, 20, 101483. doi:10.1016/j.rineng.2023.101483.

Appendix I

Responses	Source	DF	Adj SS	Adj MS	F-Value	P-Value	Responses	Source	DF	Adj SS	Adj MS	F-Value	P-Value
SCF 0°	Model	18	27.3461	1.51923	350.26	<0.001	SCF 10°	Model	17	28.9016	1.7001	366.72	<0.001
	Linear	8	14.3361	1.79201	413.16	<0.001		Linear	8	14.8844	1.8605	401.33	<0.001
	β	1	1.2509	1.25091	288.40	<0.001		β	1	1.2278	1.2278	264.84	<0.001
	γ	1	1.3000	1.30000	299.72	<0.001		γ	1	1.3223	1.3223	285.23	<0.001
	τ	1	9.8422	9.84219	2269.16	<0.001		τ	1	10.1754	10.1754	2194.89	<0.001
	θ	1	0.0953	0.09526	21.96	<0.001		θ	1	0.0786	0.0786	16.95	<0.001
	ζ	1	0.4223	0.42232	97.37	<0.001		ζ	1	0.2701	0.2701	58.26	<0.001
	λ	1	1.1469	1.14694	264.43	<0.001		λ	1	1.3843	1.3843	298.59	<0.001
	δ	1	1.9221	1.92215	443.16	<0.001		δ	1	2.0354	2.0354	439.04	<0.001
	ψ	1	0.7986	0.79861	184.12	<0.001		ψ	1	0.8434	0.8434	181.93	<0.001
	Square	2	0.1841	0.09207	21.23	<0.001		Square	2	0.1517	0.0759	16.36	<0.001
	ζ*ζ	1	0.1661	0.16608	38.29	<0.001		ζ*ζ	1	0.1033	0.1033	22.29	<0.001
	λ*λ	1	0.0181	0.01805	4.16	0.043		λ*λ	1	0.0484	0.0484	10.44	0.001
	2-Way Interaction	8	2.6943	0.33679	77.65	<0.001		2-Way Interaction	7	2.8132	0.4019	86.69	<0.001
	β*λ	1	0.0241	0.02405	5.55	0.020		β*λ	1	0.0201	0.0201	4.33	0.039
	β*δ	1	0.0358	0.03580	8.25	0.005		β*δ	1	0.0374	0.0374	8.06	0.005
	γ*δ	1	0.0206	0.02064	4.76	0.031		γ*δ	1	0.0272	0.0272	5.87	0.016
	τ*δ	1	0.3676	0.36763	84.76	<0.001		τ*δ	1	0.3656	0.3656	78.86	<0.001
	τ*ψ	1	0.0448	0.04476	10.32	0.002		τ*ψ	1	0.0541	0.0541	11.67	0.001
	λ*δ	1	1.8363	1.83632	423.37	<0.001		λ*δ	1	1.9831	1.9831	427.78	<0.001
λ*ψ	1	0.2921	0.29207	67.34	<0.001	λ*ψ	1	0.2744	0.2744	59.18	<0.001		
δ*ψ	1	0.0211	0.02106	4.86	0.029								
SCF 20°	Model	18	31.3326	1.7407	398.49	<0.001	SCF 30°	Model	20	33.8541	1.6927	524.46	<0.001
	Linear	8	16.9691	2.1211	485.58	<0.001		Linear	8	15.9089	1.9886	616.14	<0.001
	β	1	1.1220	1.1220	256.86	<0.001		β	1	1.2143	1.2143	376.24	<0.001
	γ	1	1.5753	1.5753	360.62	<0.001		γ	1	2.2809	2.2809	706.71	<0.001
	τ	1	10.9844	10.9844	2514.61	<0.001		τ	1	11.0438	11.0438	3421.74	<0.001
	θ	1	0.0440	0.0440	10.08	0.002		θ	1	0.0145	0.0145	4.49	0.036
	ζ	1	0.0371	0.0371	8.50	0.004		ζ	1	0.0256	0.0256	7.92	0.006
	λ	1	2.2423	2.2423	513.33	<0.001		λ	1	1.1728	1.1728	363.36	<0.001
	δ	1	2.1624	2.1624	495.04	<0.001		δ	1	2.2403	2.2403	694.11	<0.001
	ψ	1	0.9329	0.9329	213.56	<0.001		ψ	1	1.0423	1.0423	322.94	<0.001
	Square	2	0.1405	0.0702	16.08	<0.001		Square	3	0.0624	0.0208	6.45	<0.001
	λ*λ	1	0.1088	0.1088	24.92	<0.001		ζ*ζ	1	0.0148	0.0148	4.58	0.034
	ψ*ψ	1	0.0316	0.0316	7.24	0.008		λ*λ	1	0.0329	0.0329	10.19	0.002
	2-Way Interaction	8	2.9142	0.3643	83.39	<0.001		ψ*ψ	1	0.0148	0.0148	4.57	0.034
	β*δ	1	0.0519	0.0519	11.89	0.001		2-Way Interaction	9	2.7036	0.3004	93.07	<0.001
	γ*λ	1	0.0198	0.0198	4.54	0.035		β*λ	1	0.0964	0.0964	29.87	<0.001
	γ*δ	1	0.0222	0.0222	5.09	0.025		β*δ	1	0.0954	0.0954	29.56	<0.001
	τ*δ	1	0.3943	0.3943	90.27	<0.001		γ*δ	1	0.0135	0.0135	4.19	0.042
	τ*ψ	1	0.0579	0.0579	13.26	<0.001		γ*ψ	1	0.0285	0.0285	8.82	0.003
	ζ*δ	1	0.0178	0.0178	4.06	0.045		τ*δ	1	0.4397	0.4397	136.25	<0.001
λ*δ	1	2.0380	2.0380	466.55	<0.001	τ*ψ	1	0.1083	0.1083	33.56	<0.001		
λ*ψ	1	0.2489	0.2489	56.97	<0.001	ζ*δ	1	0.0394	0.0394	12.19	0.001		
						λ*δ	1	1.4457	1.4457	447.91	<0.001		
						λ*ψ	1	0.3543	0.3543	109.79	<0.001		

SCF 40°	Model	21	34.6417	1.6496	800.21	<0.001	Model	26	44.8314	1.72428	1821.45	<0.001
	Linear	7	15.3780	2.1969	1065.68	<0.001	Linear	8	15.1688	1.89610	2002.96	<0.001
	β	1	1.0259	1.0259	497.65	<0.001	β	1	0.5537	0.55374	584.95	<0.001
	γ	1	3.1475	3.1475	1526.82	<0.001	γ	1	2.2356	2.23560	2361.59	<0.001
	τ	1	10.7795	10.7795	5229.05	<0.001	τ	1	9.5603	9.56029	10099.04	<0.001
	ζ	1	0.1810	0.1810	87.81	<0.001	θ	1	0.0002	0.00015	0.16	0.005
	λ	1	0.0006	0.0006	0.31	0.05	ζ	1	0.3316	0.33162	350.31	<0.001
	δ	1	2.6138	2.6138	1267.94	<0.001	λ	1	0.0174	0.01741	18.39	<0.001
	ψ	1	0.9755	0.9755	473.18	<0.001	δ	1	3.6626	3.66258	3868.98	<0.001
	Square	3	0.9473	0.3158	153.18	<0.001	ψ	1	0.7063	0.70631	746.11	<0.001
	$\zeta^*\zeta$	1	0.0711	0.0711	34.50	<0.001	Square	4	5.3130	1.32825	1403.10	<0.001
	$\lambda^*\lambda$	1	0.8323	0.8323	403.74	<0.001	$\theta^*\theta$	1	0.0038	0.00380	4.01	0.047
	$\psi^*\psi$	1	0.0439	0.0439	21.30	<0.001	$\zeta^*\zeta$	1	0.0454	0.04544	48.00	<0.001
	2-Way Interaction	11	2.4204	0.2200	106.74	<0.001	$\lambda^*\lambda$	1	5.1678	5.16777	5458.98	<0.001
	$\beta^*\lambda$	1	0.1346	0.1346	65.30	<0.001	$\psi^*\psi$	1	0.0479	0.04793	50.63	<0.001
	$\beta^*\delta$	1	0.1124	0.1124	54.54	<0.001	2-Way Interaction	14	1.7163	0.12259	129.50	<0.001
	$\beta^*\psi$	1	0.0248	0.0248	12.02	0.001	$\beta^*\lambda$	1	0.0176	0.01760	18.59	<0.001
	$\gamma^*\lambda$	1	0.0902	0.0902	43.74	<0.001	$\beta^*\delta$	1	0.0606	0.06056	63.98	<0.001
	$\gamma^*\delta$	1	0.0125	0.0125	6.05	0.015	$\beta^*\psi$	1	0.0319	0.03185	33.65	<0.001
	$\tau^*\lambda$	1	0.0254	0.0254	12.32	0.001	$\gamma^*\delta$	1	0.0370	0.03705	39.14	<0.001
$\tau^*\delta$	1	0.4780	0.4780	231.86	<0.001	$\gamma^*\psi$	1	0.0131	0.01308	13.82	<0.001	
$\tau^*\psi$	1	0.1289	0.1289	62.51	<0.001	$\tau^*\lambda$	1	0.0017	0.00174	1.84	0.177	
$\zeta^*\delta$	1	0.0700	0.0700	33.94	<0.001	$\tau^*\delta$	1	0.5621	0.56208	593.75	<0.001	
$\lambda^*\delta$	1	0.9162	0.9162	444.42	<0.001	$\tau^*\psi$	1	0.0774	0.07737	81.73	<0.001	
$\lambda^*\psi$	1	0.2903	0.2903	140.84	<0.001	$\theta^*\delta$	1	0.0036	0.00361	3.81	0.05	
SCF 60°	Model	21	54.6828	2.6039	500.95	<0.001	Model	21	56.5541	2.6931	577.14	<0.001
	Linear	8	19.4521	2.4315	467.78	<0.001	Linear	8	21.7801	2.7225	583.45	<0.001
	β	1	0.2141	0.2141	41.18	<0.001	β	1	0.1531	0.1531	32.82	<0.001
	γ	1	2.2259	2.2259	428.22	<0.001	γ	1	4.6210	4.6210	990.31	<0.001
	τ	1	11.0083	11.0083	2117.78	<0.001	τ	1	10.4195	10.4195	2232.97	<0.001
	θ	1	0.0192	0.0192	3.70	0.05	θ	1	0.0270	0.0270	5.79	0.017
	ζ	1	0.4924	0.4924	94.73	<0.001	ζ	1	0.6606	0.6606	141.57	<0.001
	λ	1	0.0137	0.0137	2.64	0.001	λ	1	0.2931	0.2931	62.80	<0.001
	δ	1	4.7972	4.7972	922.89	<0.001	δ	1	5.7585	5.7585	1234.09	<0.001
	ψ	1	2.3051	2.3051	443.45	<0.001	ψ	1	2.0282	2.0282	434.65	<0.001
	Square	3	9.1909	3.0636	589.39	<0.001	Square	3	1.0403	0.3468	74.31	<0.001
	$\zeta^*\zeta$	1	0.0874	0.0874	16.82	<0.001	$\zeta^*\zeta$	1	0.0984	0.0984	21.08	<0.001
	$\lambda^*\lambda$	1	9.0196	9.0196	1735.20	<0.001	$\lambda^*\lambda$	1	0.7780	0.7780	166.73	<0.001
	$\psi^*\psi$	1	0.0839	0.0839	16.14	<0.001	$\psi^*\psi$	1	0.1639	0.1639	35.13	<0.001
	2-Way Interaction	10	1.5847	0.1585	30.49	<0.001	2-Way Interaction	10	1.7951	0.1795	38.47	<0.001
	$\beta^*\delta$	1	0.0460	0.0460	8.86	0.003	$\beta^*\delta$	1	0.0498	0.0498	10.68	0.001
	$\gamma^*\delta$	1	0.0550	0.0550	10.58	0.001	$\beta^*\psi$	1	0.0311	0.0311	6.67	0.011
	$\gamma^*\psi$	1	0.0258	0.0258	4.97	0.027	$\gamma^*\lambda$	1	0.0307	0.0307	6.57	0.011
	$\tau^*\delta$	1	0.5622	0.5622	108.15	<0.001	$\gamma^*\delta$	1	0.0822	0.0822	17.61	<0.001
	$\tau^*\psi$	1	0.2246	0.2246	43.20	<0.001	$\gamma^*\psi$	1	0.2001	0.2001	42.87	<0.001
$\zeta^*\delta$	1	0.1702	0.1702	32.75	<0.001	$\tau^*\delta$	1	0.6643	0.6643	142.37	<0.001	
$\zeta^*\psi$	1	0.0119	0.0119	2.29	0.002	$\tau^*\psi$	1	0.1957	0.1957	41.94	<0.001	
$\lambda^*\delta$	1	0.3676	0.3676	70.71	<0.001	$\zeta^*\delta$	1	0.2146	0.2146	45.98	<0.001	
$\lambda^*\psi$	1	0.0431	0.0431	8.28	0.005	$\lambda^*\delta$	1	0.1524	0.1524	32.67	<0.001	
$\delta^*\psi$	1	0.0513	0.0513	9.86	0.002	$\delta^*\psi$	1	0.0945	0.0945	20.25	<0.001	
SCF 70°	Model	21	34.6417	1.6496	800.21	<0.001	Model	26	44.8314	1.72428	1821.45	<0.001
	Linear	7	15.3780	2.1969	1065.68	<0.001	Linear	8	15.1688	1.89610	2002.96	<0.001
	β	1	1.0259	1.0259	497.65	<0.001	β	1	0.5537	0.55374	584.95	<0.001
	γ	1	3.1475	3.1475	1526.82	<0.001	γ	1	2.2356	2.23560	2361.59	<0.001
	τ	1	10.7795	10.7795	5229.05	<0.001	τ	1	9.5603	9.56029	10099.04	<0.001
	ζ	1	0.1810	0.1810	87.81	<0.001	θ	1	0.0002	0.00015	0.16	0.005
	λ	1	0.0006	0.0006	0.31	0.05	ζ	1	0.3316	0.33162	350.31	<0.001
	δ	1	2.6138	2.6138	1267.94	<0.001	λ	1	0.0174	0.01741	18.39	<0.001
	ψ	1	0.9755	0.9755	473.18	<0.001	δ	1	3.6626	3.66258	3868.98	<0.001
	Square	3	0.9473	0.3158	153.18	<0.001	ψ	1	0.7063	0.70631	746.11	<0.001
	$\zeta^*\zeta$	1	0.0711	0.0711	34.50	<0.001	Square	4	5.3130	1.32825	1403.10	<0.001
	$\lambda^*\lambda$	1	0.8323	0.8323	403.74	<0.001	$\theta^*\theta$	1	0.0038	0.00380	4.01	0.047
	$\psi^*\psi$	1	0.0439	0.0439	21.30	<0.001	$\zeta^*\zeta$	1	0.0454	0.04544	48.00	<0.001
	2-Way Interaction	11	2.4204	0.2200	106.74	<0.001	$\lambda^*\lambda$	1	5.1678	5.16777	5458.98	<0.001
	$\beta^*\lambda$	1	0.1346	0.1346	65.30	<0.001	$\psi^*\psi$	1	0.0479	0.04793	50.63	<0.001
	$\beta^*\delta$	1	0.1124	0.1124	54.54	<0.001	2-Way Interaction	14	1.7163	0.12259	129.50	<0.001
	$\beta^*\psi$	1	0.0248	0.0248	12.02	0.001	$\beta^*\lambda$	1	0.0176	0.01760	18.59	<0.001
	$\gamma^*\lambda$	1	0.0902	0.0902	43.74	<0.001	$\beta^*\delta$	1	0.0606	0.06056	63.98	<0.001
	$\gamma^*\delta$	1	0.0125	0.0125	6.05	0.015	$\beta^*\psi$	1	0.0319	0.03185	33.65	<0.001
	$\tau^*\lambda$	1	0.0254	0.0254	12.32	0.001	$\gamma^*\delta$	1	0.0370	0.03705	39.14	<0.001
$\tau^*\delta$	1	0.4780	0.4780	231.86	<0.001	$\gamma^*\psi$	1	0.0131	0.01308	13.82	<0.001	
$\tau^*\psi$	1	0.1289	0.1289	62.51	<0.001	$\tau^*\lambda$	1	0.0017	0.00174	1.84	0.177	
$\zeta^*\delta$	1	0.0700	0.0700	33.94	<0.001	$\tau^*\delta$	1	0.5621	0.56208	593.75	<0.001	
$\lambda^*\delta$	1	0.9162	0.9162	444.42	<0.001	$\tau^*\psi$	1	0.0774	0.07737	81.73	<0.001	
$\lambda^*\psi$	1	0.2903	0.2903	140.84	<0.001	$\theta^*\delta$	1	0.0036	0.00361	3.81	0.05	

SCF 80°	Model	18	62.0370	3.4465	378.70	<0.001	SCF 90°	Model	17	80.5092	4.73583	259.16	<0.001
	Linear	7	35.1863	5.0266	552.32	<0.001		Linear	7	34.0750	4.86785	266.39	<0.001
	γ	1	4.4918	4.4918	493.56	<0.001		β	1	5.2281	5.22811	286.10	<0.001
	τ	1	9.1894	9.1894	1009.73	<0.001		γ	1	5.5708	5.57080	304.85	<0.001
	θ	1	0.1112	0.1112	12.22	0.001		τ	1	5.3437	5.34370	292.43	<0.001
	ζ	1	0.7867	0.7867	86.44	<0.001		ζ	1	0.6550	0.65496	35.84	<0.001
	λ	1	1.0754	1.0754	118.17	<0.001		λ	1	2.9423	2.94233	161.01	<0.001
	δ	1	16.7917	16.7917	1845.07	<0.001		δ	1	8.4323	8.43226	461.44	<0.001
	ψ	1	4.8683	4.8683	534.93	<0.001		ψ	1	2.2728	2.27278	124.37	<0.001
	Square	3	0.6052	0.2017	22.17	<0.001		Square	1	0.3340	0.33400	18.28	<0.001
	$\zeta^*\zeta$	1	0.0525	0.0525	5.77	0.017		$\gamma^*\gamma$	1	0.3340	0.33400	18.28	<0.001
	$\lambda^*\lambda$	1	0.3932	0.3932	43.21	<0.001		2-Way Interaction	9	4.4503	0.49448	27.06	<0.001
	$\psi^*\psi$	1	0.1594	0.1594	17.52	<0.001		$\beta^*\delta$	1	0.0982	0.09816	5.37	0.022
	2-Way Interaction	8	1.9571	0.2446	26.88	<0.001		$\beta^*\psi$	1	0.4460	0.44597	24.41	<0.001
	$\gamma^*\lambda$	1	0.2063	0.2063	22.67	<0.001		$\gamma^*\lambda$	1	0.0937	0.09367	5.13	0.025
	$\gamma^*\psi$	1	0.5232	0.5232	57.49	<0.001		$\gamma^*\psi$	1	1.3554	1.35540	74.17	<0.001
	$\tau^*\lambda$	1	0.1167	0.1167	12.82	<0.001		$\tau^*\delta$	1	0.6476	0.64757	35.44	<0.001
	$\tau^*\delta$	1	0.6070	0.6070	66.69	<0.001		$\tau^*\psi$	1	0.3745	0.37451	20.49	<0.001
$\tau^*\psi$	1	0.2096	0.2096	23.04	<0.001	$\zeta^*\delta$	1	0.2774	0.27744	15.18	<0.001		
$\theta^*\lambda$	1	0.0459	0.0459	5.04	0.026	$\lambda^*\psi$	1	0.2869	0.28687	15.70	<0.001		
$\zeta^*\delta$	1	0.2751	0.2751	30.23	<0.001	$\delta^*\psi$	1	0.1177	0.11768	6.44	0.012		
$\delta^*\psi$	1	0.1253	0.1253	13.77	<0.001								
SCF Peak	Model	22	44.6679	2.0304	202.82	<0.001							
	Linear	7	20.7100	2.9586	295.55	<0.001							
	β	1	0.3729	0.3729	37.25	<0.001							
	γ	1	5.1860	5.1860	518.05	<0.001							
	τ	1	11.4497	11.4497	1143.76	<0.001							
	ζ	1	0.1051	0.1051	10.50	0.001							
	λ	1	0.3212	0.3212	32.09	<0.001							
	δ	1	3.6746	3.6746	367.08	<0.001							
	ψ	1	2.0319	2.0319	202.97	<0.001							
	Square	3	0.7642	0.2547	25.45	<0.001							
	$\gamma^*\gamma$	1	0.0619	0.0619	6.18	0.014							
	$\lambda^*\lambda$	1	0.5109	0.5109	51.03	<0.001							
	$\psi^*\psi$	1	0.1914	0.1914	19.12	<0.001							
	2-Way Interaction	12	4.4459	0.3705	37.01	<0.001							
	$\beta^*\delta$	1	0.2330	0.2330	23.27	<0.001							
	$\beta^*\psi$	1	0.2023	0.2023	20.21	<0.001							
	$\gamma^*\lambda$	1	0.2335	0.2335	23.33	<0.001							
	$\gamma^*\delta$	1	0.2288	0.2288	22.85	<0.001							
	$\gamma^*\psi$	1	0.3819	0.3819	38.15	<0.001							
	$\tau^*\delta$	1	0.5103	0.5103	50.97	<0.001							
	$\zeta^*\lambda$	1	0.0736	0.0736	7.35	0.007							
$\zeta^*\delta$	1	0.2908	0.2908	29.05	<0.001								
$\zeta^*\psi$	1	0.0887	0.0887	8.86	0.003								
$\lambda^*\delta$	1	0.8905	0.8905	88.96	<0.001								
$\lambda^*\psi$	1	0.6438	0.6438	64.31	<0.001								
$\delta^*\psi$	1	0.3535	0.3535	35.31	<0.001								